İSTANBUL TECHNICAL UNIVERSITY ★ INSTITUTE OF SCIENCE AND TECHNOLOGY

MICROMEGAS AND GEM DETECTORS FOR THE FUTURE CANDIDATES OF CERN-SLHC ATLAS EXPERIMENT

M.Sc. Thesis by
Sinem ŞALVA

Department : Physics Engineering

Programme : Physics Engineering

JUNE 2010

İSTANBUL TECHNICAL UNIVERSITY ★ INSTITUTE OF SCIENCE AND TECHNOLOGY

MICROMEGAS AND GEM DETECTORS FOR THE FUTURE CANDIDATES OF CERN-SLHC ATLAS EXPERIMENT

M.Sc. Thesis by
Sinem ŞALVA
(509071114)

Date of submission : 07 May 2010
Date of defence examination: 23 June 2010

Supervisor (Chairman) : Prof. Dr. Cenap Ş. ÖZBEN (ITU)
Members of the Examining Committee : Prof. Dr. Metin ARIK (BU)
Doç. Dr. Kerem CANKOÇAK (ITU)

JUNE 2010

İSTANBUL TEKNİK ÜNİVERSİTESİ ★ FEN BİLİMLERİ ENSTİTÜSÜ

CERN-SLHC ATLAS DENEYİNİN GELECEĞİ İÇİN ÖNGÖRÜLEN MİCROMEGAS VE GEM DETEKTÖRLERİ

YÜKSEK LİSANS TEZİ

Sinem ŞALVA
(509071114)

Tezin Enstitüye Verildiği Tarih : 07 Mayıs 2010
Tezin Savunulduğu Tarih : 23 Haziran 2010

Tez Danışmanı : Prof. Dr. Cenap Ş. ÖZBEN (İTÜ)
Diğer Jüri Üyeleri : Prof. Dr. Metin ARIK (BÜ)
Doç. Dr. Kerem CANKOÇAK (İTÜ)

HAZİRAN 2010

FOREWORD

First, I would like to thank my supervisor Prof. Dr. Cenap ÖZBEN for his guidance, useful discussions and his support during my thesis work and for being such a friendly supervisor.

With a deep sense of gratitude, I would like to express my sincere thanks to Prof. Dr. Metin ARIK who made my work possible and drove me into the exciting corridors of physics.

I am thankful to Prof. Dr. Serkant ÇETİN for his support during my studies.

I also would like to thank Joerg WOTSCHACK and Givi SEKHNIAIDZE for their helps during my studies at CERN.

Finally, I am deeply grateful to my parents Mürüvet & Sıtkı ŞALVA and my brother Kerem ŞALVA and my grandmother Sabiha DİNDAROĞLU for their companionship, support and advices. I am also very grateful to my family, cousins, friends and Faruk DİBLEN for their supports and taking part in my life.

June 2010

Sinem ŞALVA
Physics Engineer

TABLE OF CONTENTS

Page

ABBREVIATIONS

ADC	**:** Analog-to-Digital converter
ALICE	**:** A Large Ion Collider Experiment
ATLAS	**:** A Toroidal LHC Apparatus
BNC	**:** Bayonet Neill-Concelman connector
CMS	**:** Compact Muon Solenoid
CSC	**:** Cathode Strip Chamber
DAQ	**:** Data Acquisition
ECAL/ECal	**:** Electromagnetic Calorimeter
FWHM	**:** Full Width at Half Maximum
GEM	**:** Gas Electron Multiplier
HCAL/HCal	**:** Hadronic Calorimeter
LAr	**:** Liquid Argon
LHC	**:** Large Hadron Collider
LHC-B	**:** A dedicated LHC Beauty
LHC-F	**:** A dedicated LHC Forward
MAMMA	**:** Muon ATLAS Micromegas Activity
MDT	**:** Monitored Drift Tubes
MICROMEGAS	**:** Micromesh Gaseous Structure
MM	**:** MicroMegas
MSGC	**:** Microstrip Gas Chamber
MPGD	**:** Micro Pattern Gas Detector
MWPC	**:** Multiwire Proportional Chamber
PCB	**:** Printed-Circuit Board
PPAC	**:** Parallel-Plate Avalanche Counter
RPC	**:** Resistive Plate Chamber
SCT	**:** Semiconductor Tracker (of the ATLAS experiment)
SLHC	**:** Super Large Hadron Collider
SM	**:** Standard Model
SUSY	**:** Supersymmetry
SWPC	**:** Single Wire Proportional Chamber
TGC	**:** Thin Gap Chamber
TOTEM	**:** A TOTal and Elastic Measurement Experiment
TRT	**:** Transition Radiation Tracker (of the ATLAS experiment)

LIST OF TABLES

Page

LIST OF FIGURES

Page

LIST OF SYMBOLES

V_D : The voltage of drift electrode
V_M : The voltage of mesh
V_{GEM} : The voltage of GEM
V_{GB} : The voltage of the bottom side of GEM
V_{GT} : The voltage of the top side of GEM
E_{amp} : Electric field of the amplification gap
E_{drift} : Electric field of the conversion gap
pf : Picofarad
l : Litre
h : Hour
Ω : Ohm
Min : Minimum
Max : Maximum
ΔV_{GEM} : Voltage difference between the top side of GEM and the bottom side of the GEM
I : Current
Δt : Average time
mA : Milliampere
Bq : Becquerel
Q_e : $1{,}6 \cdot 10^{-19}$ Coulomb
C : Capacitance
ns : Nanosecond
HV : High-voltage
G_{GAS} : Gas gain
G : Gain

MICROMEGAS AND GEM DETECTORS FOR THE FUTURE CANDIDATES OF CERN-SLHC ATLAS EXPERIMENT

SUMMARY

The world's largest particle physics laboratory CERN switches on the Large Hadron Collider (LHC), designes to search new physics and new particles including Higgs boson, dark matter, dark energy, extra dimensions, supersymmetry, matter and antimatter. After the LHC works for a while, an upgrade is needed for the renovations with running experiences and extra needs. The ATLAS is one of the detectors constructed at the LHC and it has the largest volume in the experiment. The Muon system of the ATLAS experiment is also needed a detector upgrade in the highest rapidity region. Muon Spectrometer is the largest part of the ATLAS detector, and Cathode Strip Chamber (CSC) which is a part of the Muon system has new technology detector candidates instead of it. In this thesis, The Micro Pattern Gas Detectors (MPGD) are introduced as the candidates for the upgrade. Since the improvement of MPGDs, an extensive research is started to understand the new detector generation and optimize it for the needs of high energy physics or the other applications. Nowadays the two more are developed MPGDs technologies are Gas Electron Multiplier (GEM) and Micromesh Gaseous Structure (Micromegas). For future SLHC (Super LHC), one of the most challenging objective is the realization of large area MPGDs. Muon Atlas Micromegas Activity is an ongoing R&D group with the aim to develop large detectors based on the microbulk-Micromegas technology to use in the ATLAS Muon Spectrometer. Micromegas is a good potential candidate for the construction of large muon chambers that combine trigger and tracking capability and can sustain high particle rates expected at the SLHC. GEM detector also has many advantages especially to use in high energy and medical physics. GEM has very high radiation rate capability, high performance at low cost, flexible detector shape, readout patterns, good energy resolution and spatial resolution. The performance tests of Micromegas and GEM, also some laboratory measurements are determined with this work. The different kinds of voltage scans are performed to understand voltage-gain relation of the detector, and the optimum values of the voltages and electric fields are determined by changing the voltages according to the scans. On the other hand, the test-beam which is done to test the detectors at CERN is mentioned, and the basics of the test-beam data analysis are introduced. Gamma_2 function is also mentioned which is used for the analysis of the data and it is a special function used for the fitting the data. The expected results are reached, the gain is obtained for the different voltage scans and it reaches upto 10^4 which is the ratio between the total electrons and the primary electrons created in the detector. The gaseous detectors in new technologies are very suitable to use in high energy physics, also medical physics and other applications.

CERN-SLHC ATLAS DENEYİ DETEKTÖRLERİNDEN MICROMEGAS VE GEM'İN İNCELENMESİ

ÖZET

Dünyanın en büyük parçacık fiziği laboratuvarı olan CERN'de karanlık maddeden, anti maddeye, ekstra boyutlara, süpersimetrik parçacıklardan, maddeye kütle kazandırdığı öngörülen Higgs bozonuna kadar daha bir çok bilinmeyeni aramak için inşa edilen LHC (Büyük Hadron Çarpıştırıcısı) çalışmaya başlamıştır. Daha uzun yıllar çalışmaya devam edecek olan LHC'nin ilerleyen yıllarda gelişen teknoloji ile birlikte güncellenmeye ve yenilenmeye ihtiyacı olacaktır. ATLAS detektörü Büyük Hadron Çarpıştırıcısı'nın belli kısımlarına yerleştirilmiş olan detektörlerden hacim olarak en büyüğüdür. ATLAS detektörünün alt detektörlerinden olan Muon kısmının da bu güncellenme aşamasında yenilenmesi gerekecektir. Muon Spektrometre ATLAS'ın en büyük kısmıdır ve Katot Şeritli Odacıklar (CSC), Muon kısmının bölümlerinden biridir. Bu tezde Mikro Modelde Gazlı Detektörlerden (MPGD) ve deneyin güncellenme aşamasında Katot Şeritli Odacıklar kısmı için kullanılmaya aday olan yeni nesil MPGD çeşitlerinden Micromegas ve GEM incelenmiştir. Son yıllarda MPGD geliştirilerek yüksek enerji fiziğine ve diğer fizik dallarına katkısı oldukça etkili hale gelmiştir ve Micromegas ile GEM detektörleri güçlü örnekler olmuştur. SLHC (Super LHC) için en etkili aday detektörler içerisinde yer almaktadırlar. Muon Atlas Micromegas Aktivite grubu Muon Spektrometre kısmında kullanılmak üzere Micromegas detektörünü geliştirme çalışmalarını sürdürmektedir. Micromegas, tetikleme ve iz sürme işlemlerini birlikte yapabilme kapasitesine sahip, SLHC'de çok yüksek parçacık değerlerine ulaşıldığında istenilen ölçümleri yapabilecek bir detektördür. GEM ise düşük maliyetlerde yüksek performansa sahip, çözünürlüğü yüksek, esnek ölçeklere sahip birçok avantaja sahip bir gazlı detektördür. Bu tezdeki çalışmalar boyunca Micromegas ve ayrıca içerisine GEM yerleştirilerek bu detektörlerin performans testleri yapılmıştır. Detektörlere yüksek gerilimler uygulanarak elektrik alan ve gerilim verileri için optimum değerler belirlenmiştir. Detektörleri test etmek için periyodik olarak CERN'de yapılan Test-beam süreçlerinden ve bu süreçlerde alınan verilerin analizine değinilmiştir. Gamma_2 Fonksiyonu adındaki özel bir fonksiyon ile verinin nasıl fit edildiği vurgulanmıştır. Gerilim ile ilgili taramalarda ise elde edilen gain değerleri tespit edilmiş ve 10^4 mertebesine kadar ulaşıldığı gözlemlenmiştir. Detektörden elde edilen toplam elektron sayısının, birincil elektronlara oranı gain değerini vermektedir. Elde edilen sonuçlar beklendiği gibidir, ve yeni nesil gazlı detekörler yüksek enerji fiziği dışında başta medikal fizik olmak üzere pek çok alanda kullanılmaya elverişlidir.

1. INTRODUCTION

The physics dedicated to the study of the fundamental constituents of matter and their interactions is called particle physics. The Standard Model of particle physics describes the interactions between elementary particles. It predicts a particle called the Higgs Boson, that provides an answer to the question:"Where does the mass of particles originate from?" [1] To fill in the missing knowledge requires experimental data, and the next big step to achieving this is with LHC (Large Hadron Collider).

1.1 Large Hadron Collider

The LHC is the world's largest and most powerful particle accelerator. It mainly consists of a 27 km ring of superconducting magnets with a number of accelerating structures to boost the energy of the particles along the way.

Inside the accelerator, two beams of particles travel at close to the speed of light with very high energies before colliding with one another. The beams travel in opposite directions in separate beam pipes where they kept at ultrahigh vacuum. They are guided around the accelerator ring by a strong magnetic field, achieved using superconducting electromagnets. These are built from coils of special electric cable that operates in a superconducting state, efficiently conducting electricity without resistance or loss of energy. This requires chilling the magnets to about -271 °C a temperature colder than outer space. For this reason, much of the accelerator is connected to a distribution system of liquid helium, which cools the magnets, as well as to other supply services. Thousands of magnets of different varieties and sizes are used to direct the beams around the accelerator. These include 1232 dipole magnets of 15 m length which are used to bend the beams, and also 392 quadrupole magnets, each of them almost 5-7 m long, and they are used to focus the beams. On the other hand another type of magnet is used to focus the particles to increase the chances of collisions. The magnet coils are made of copper-clad niobium-titanium cables. The cryogenic technology chosen for the LHC uses superfluid helium which has efficient heat transfer properties.

The first beam was circulated through the collider on the morning of 10 September 2008. CERN successfully fired the first proton around the entire tunnel circuit in stages. The particles were fired in a clockwise direction into the accelerator and successfully steered around it, and CERN next successfully sent a beam of protons in a counterclockwise direction.

On 19 September 2008, a quench occurred in about 100 bending magnets in sectors 3 and 4, causing a loss of approximately six tonnes of liquid helium, which was vented into the tunnel, and a temperature rise of about 100K in some of the affected magnets. Vacuum conditions in the beam pipe were also lost. Shortly after the incident CERN reported that the most likely cause of the problem was a faulty electrical connection between two magnets. A total of 53 magnets were damaged in the incident and were repaired or replaced during the winter shutdown.

After this period, low energy beams circulated in the tunnel for the first time since the incident on 20 November 2009, and the first particle collisions in all 4 detectors at 450 GeV on 23 November 2009. On 30 November 2009, LHC becomes the world's highest energy particle accelerator achieving 1.18 TeV per beam, beating the Tevatron's previous record of 0.98 TeV per beam held for 8 years.

On 30 March 2010, LHC set a record for high-energy collisions, by colliding proton beams at a combined energy level of 7 TeV. CERN will run the LHC for 18–24 months with the objective of delivering enough data to the experiments to make significant advances across a wide range of physics channels. After this period it will be shut down to prepare for the 14 TeV collisions (7 TeV per beam) [2].

1.1.1 The parts of the LHC

The experiments at the LHC are all run by international collaborations, bringing together scientists from institutes all over the world. Each experiment is distinct, characterised by its unique particle detector and magnet system. The two large experiments, ATLAS (A Toroidal LHC Apparatus) and CMS (Compact Muon Solenoid), are based on general purpose detectors to analyses the myriad of particles produced by the collisions in the accelerator. They are designed to investigate the largest range of physics with the same scientific goals by using different technical solutions. Having two independently designed detectors is vital for cross-confirmation of any new discoveries made.

Two medium-size experiments, ALICE (A Large Ion Collider) and LHC-B (LHC-Beauty), have specialised detectors for analysing the LHC collisions in relation to specific phenomena as heavy ion collisions and bottom quark physics respectively. Two experiments, TOTEM (A TOTal and Elastic Measurement Experiment) and LHC-F (LHC-Forward), are much smaller in size. LHC-F is designed to focus on forward particles which are protons or heavy ions and the cosmic ray physics (origin of ultra-high energy cosmic rays). TOTEM is designed to search about the total cross section and elastic scattering. These are particles that just brush past each other as the beams collide, rather than meeting head-on. The ATLAS, CMS, ALICE and LHC-B detectors are installed in four huge underground caverns located around the ring of the LHC. The detectors used by the TOTEM experiment are positioned near the CMS detector, whereas those used by LHC-F are near the ATLAS detector [3]. The schematic aspect of the LHC is shown in Figure 1.1 with its subdetectors.

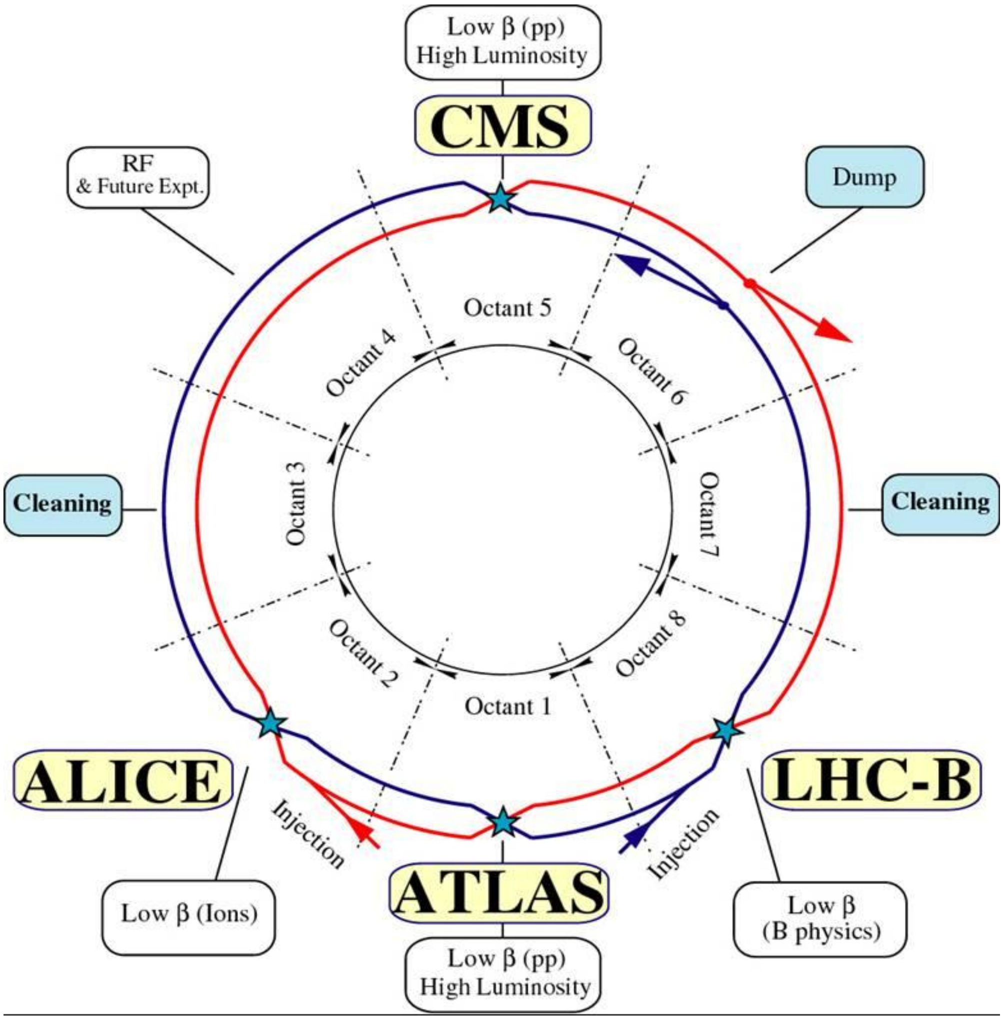

Figure 1.1 : The LHC Layout.

For the future, an upgraded LHC-the super LHC (SLHC)-delivering ten times higher instantaneous luminosity is being considered. This increase in luminosity would result in a roughly proportional increase of the expected counting rates from muons and background sources, namely photons, neutrons and protons. For the detector coverage and the good detector performance to be maintained under these conditions, it is likely that an upgrade of the present tracking and trigger chambers in the forward region will be necessary. Specifically, this applies to the Inner and Middle stations of the End-Cap Muon Spectrometer corresponding to a total surface of 400 m^2.

1.2 ATLAS Experiment

The ATLAS detector which is shown in Figure 1.2 is one of the six particle detector experiments constructed at LHC. ATLAS is 44 meters long and 25 meters in diameter, weighing about 7000 tones which is designed to study the proton-proton collisions at CERN Large Hadron Collider (LHC), at a center of mass energy of 14 TeV and bunch crossing rate of 40 MHz.

ATLAS will search for new discoveries in the head-on collisions of protons of extraordinarily high energy. ATLAS will learn about the basic forces that have shaped our Universe since the beginning of time and that will determine its fate. Among the possible unknowns are the origin of mass, extra dimensions of space, microscopic black holes, and evidence for dark matter candidates in the Universe. The ATLAS experiment offers a large physics potential by focusing on electroweak symmetry breaking, particularly the search for the Higgs boson, a hypothesized particle which, if it exists, would provide the mechanism by which particles acquire mass [4]. The configuration of the ATLAS detector is typical for experiments at particle colliders: subdetectors are arranged in the layers around the beam axis (the barrel section) and in wheels (the end-caps) that close both ends of the cylinder.

The first barrel layer, located next to the interaction point, is the Inner Detector; this apparatus is composed of three sub-detectors: (from inside to outside) the Pixel Detector, the Semi-Conductor Tracker (SCT) and the Transition Radiation Tracker (TRT). The Inner Detector is surrounded by a cryostat, which contains the Central Solenoid and the Liquid Argon (LAr) calorimeter. The Central Solenoid has a superconducting coil and generates 2 Tesla solenoidal magnetic field, oriented along the beam axis. This allows for the measurement of the momenta of charged particles in the Inner Detector. The liquid argon calorimeter is responsible for the measurement of the energy of electromagnetic showers (electrons, photons). The ATLAS calorimeter in the barrel region is completed by the TileCal calorimeter, which measures the energy deposited by showers not contained in the liquid argon calorimeter mostly caused by hadrons. The steel structure of the TileCal is used as yoke for the return flux of the solenoid.

The outermost ATLAS barrel layer is the Muon Spectrometer. The spectrometer uses a separate magnetic field, generated by eight superconducting coils deployed radially around the beam axis; the coils create a 4 Tesla toroidal magnetic field that encompasses the whole spectrometer.

The Muon Spectrometer uses in the barrel region two types of chambers: Monitored Drift Tube (MDT) chambers for precision measurements, and Resistive Plate Chambers (RPC) for triggering. The two end-caps are identical and consist of a cryostat containing the liquid argon electromagnetic and hadronic calorimeters. Behind the cryostat wheel of Cathode Strip Chambers (CSC), which are part of the trigger of the Muon Spectrometer, is located. The end-caps have their own 4 T toroidal magnetic fields generated by two eight coil toroids that put into the ATLAS barrel. The Muon Spectrometer in the end-cap region consists of MDT chambers and Thin Gap Chambers (TGC), which complete the muon trigger system. Monitored Drift Tubes and Thin Gap Chambers are mounted on wheels placed between the ATLAS endcaps and the walls of the underground experimental area. Two high density Forward Calorimeters cover the very forward region of ATLAS and enhance the hermeticity of the detector. Two beam shields connect ATLAS to the LHC accelerator and protect the end-cap instrumentation from beam radiation and RF fields [3,4].

The interactions in the ATLAS detector creates an enormous dataflow. There are three systems as the trigger system, the Data Acquisition (DAQ) system and the computing system to organize the data. The trigger system selects a hundred interesting events per second out of thousand million others. The DAQ system channels the data from the detectors to the storages. The computing system is to analyse thousand million events which are recorded per year.

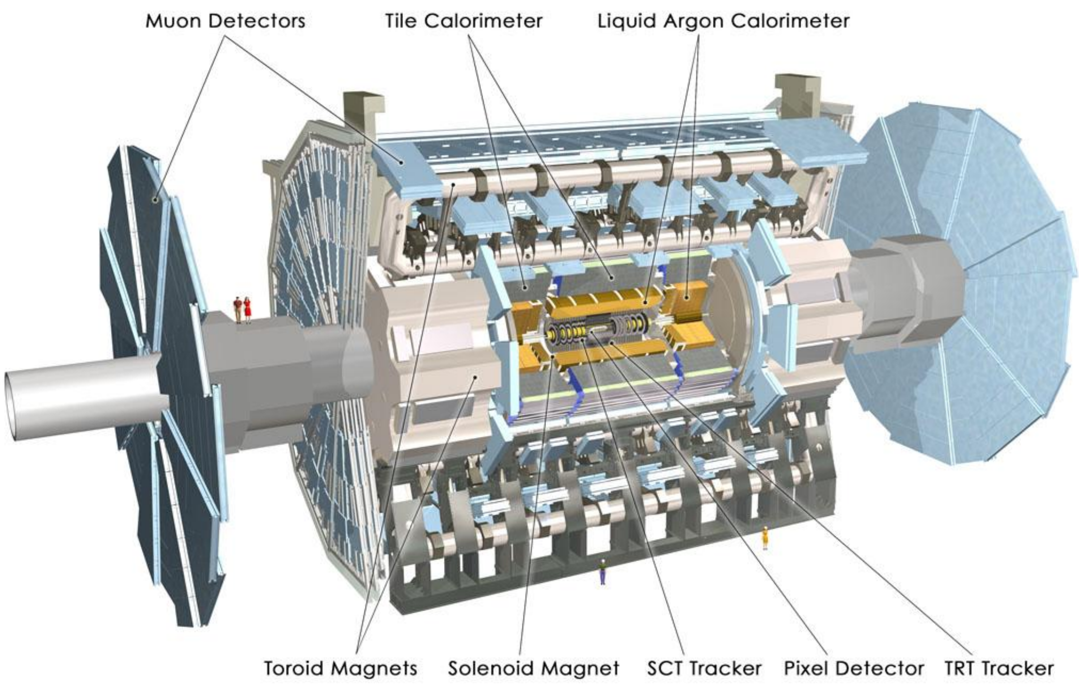

Figure 1.2 : The ATLAS Detector.

1.3 Muon Spectrometer

The outer part of the ATLAS detector consists of the muon system, where the momentum of muons escaping the calorimeters are measured. An overview of the muon system layout is given in Figure 1.3. The diameter of muon system is 22 m and the length is 48 m. In the barrel region, the muon tracks are bent in a magnetic field, which is as orthogonal to the muon trajectories as possible, and the tracks are measured by chambers arranged in three cylindrical layers. For the end-cap regions, the muon chambers are installed vertically, as wheels in three layers. MDTs measure the track coordinates. CSCs with higher granularity are used where the radiation and background levels are higher. Resistive plate chambers RPCs and thin gap chambers TGCs are installed in the barrel and end-cap regions.

The MDT chambers are placed in an aircore toroidal magnetic field, which has the advantage of little multiple scattering due to the little material present between chambers. The drawback of the design is the low magnetic field strength that can be reached. For example, a 1 TeV muon track is bent by the magnetic field such that it obtains a sagitta varying between 500 μm at rapidity η=0 (in the barrel) and 1 mm at rapidity η=2 (in the endcap). Consequently, in order to measure the momentum of a 1 TeV muon to 10%, the error of the sagitta measurement must be 50 μm.

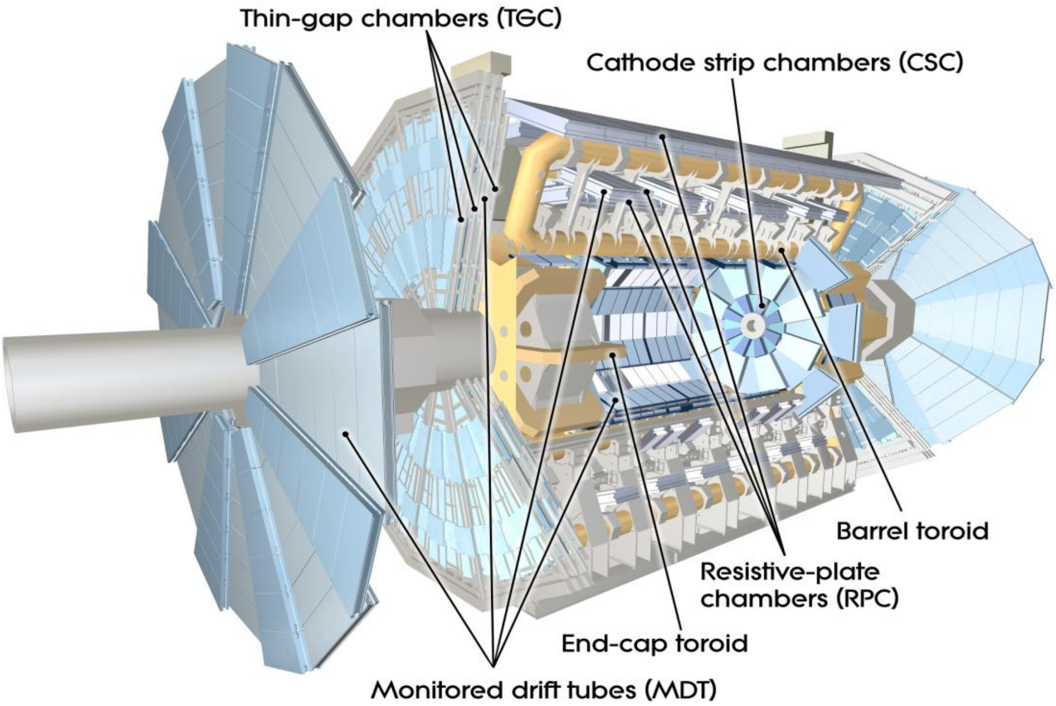

Figure 1.3 : Layout of the muon chambers. The diameter of the muon system is 22 m, the length is 46 m.

Each track is detected in three about equally spaced layers, thus the MDT resolution contributes a sagitta error of 40 μm, and the additional error from the alignment of the MDT chambers must not exceed 30-40 μm in order to meet the specification.

It is based on the magnetic deflection of muon tracks in the toroidal field and it is instrumented with separate trigger and high precision tracking chambers. High-momentum final state muons are among the most promising and robust signatures of physics at the LHC. To exploit this potential, the ATLAS Collaboration has designed a high resolution Muon Spectrometer with stand alone triggering and momentum measurement capability over a wide range of transverse momentum, pseudorapidity and azimuthal angle. The muon system design fulls some conditions like a transverse momentum resolution of 1% in the low p_T region. This limit is set by the requirement to detect the $H \rightarrow ZZ^*$ decay in the muon channel with a high suppression of the background. At the highest p_T the muon system should have sufficient momentum resolution to give good charge identification for $Z \rightarrow \mu\mu$ decay. A hermetic system is used to prevent particles escaping through holes. Measurement of spatial coordinates in two dimensions is possible to provide good mass resolution. A low rate of both punch is reached through hadrons and fake tracks.

1.4 Upgrade period of the LHC

The LHC upgrade will be in two phases, Phase 1 and Phase 2. The luminosity upgrade of the LHC foresees a luminosity increase by a factor 10 compared to the LHC for the Phase 2, and a factor 3 for the Phase 1. With the luminosity upgrade of the LHC machine, SLHC, the Muon system of the ATLAS experiment at CERN will also need a detector upgrade in the highest rapidity region. MAMMA, Muon ATLAS Micromegas Activity, is an ongoing R&D activity with the aim to develop large detectors based on the microbulk-Micromegas technology for use in the ATLAS Muon Spectrometer. Micromegas is a good potential candidate for the construction of large muon chambers that combine trigger and tracking capability and can sustain high particle rates expected at the SLHC, so Micromegas prototypes have been built and evaluated in the laboratory and in beam tests at CERN [5].

For the Muon upgrade for Phase 1, it will be added a layer of new chambers with several detection planes to increase the performance of the CSC. A large diameter and high operating pressure make MDTs unsuitable for use in areas where high counting rates are expected so CSCs are used. The principle of operation is illustrated in Figure 1.4 (this particular cathode geometry is called "Two Intermediate Strips" which improves the position linearity using capacitive charge division.)

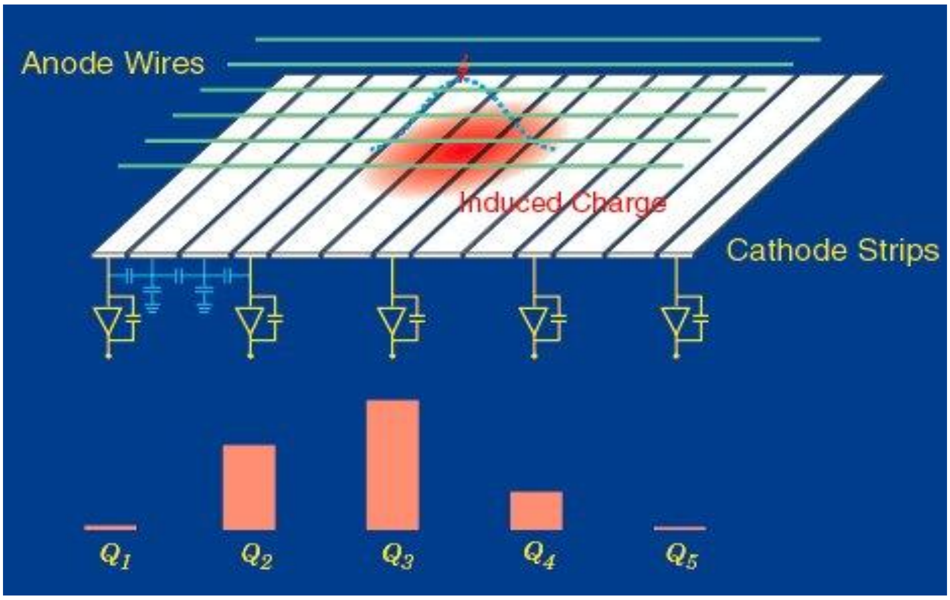

Figure 1.4 : The principle of the operation of CSC.

The avalanche around an anode wire from an ionization event creates an induced charge distribution on the cathode. The key parameter for optimum position encoding performance is the choice of the strip pitch, relative to the distance between the anode wires and the cathode plane [6,7].

However, the signal is very broad and the distance between two wires is mechanically limited. This makes it difficult to separate two nearby tracks and set limits to the possible time resolution. On the other hand, the high material budget of the support structures that hold the wires. To provide a perfectly parallel alignment the wires have to be mounted under very high tension. This demands for a very solid mounting system with a high material budget. The gating is problematic in experiments with a high event rate, where the time between two events is too short for the gating and measurement cycle. If the events do overlap, which means the drift needs longer than the time between two events, gating becomes impossible. Therefore, at high radiation levels CSC's efficiency and resolution becomes worsen due to signal overlap. The micropattern gaseous detectors are very good candidates for an upgrade, and it is referred for some kind of the micropattern gas detectors in this thesis.

2. MICROPATTERN GAS DETECTORS

In 1908 E. Rutherford and H. Geiger published the first paper on wire counters describing the use of gas amplification in the vicinity of a wire for their study of natural radioactivity [8]. In 1928, H. Geiger and W. Müller showed that the improved wire counter was sensitive to single electrons [9]. Then an exact charge measurement was made possible, when proportional tubes were made to work around 1945. G. Charpak and his collaborators made wire chambers attractive for large area applications by introducing multiwire proportional chambers for which he was honored with the 1992 Nobel Prize for Physics [10]. The age of the MPGD (Micro Pattern Gas Detectors) was introduced by A. Oed, when he demonstrated the first functional Microstrip Gas Chambers [11]. Since the improvement of MPGD, an extensive research was started to understand the new detector generation and to optimize it for the needs of high energy physics or other applications. Nowadays the two more developed MPGD thechologies are GEM [12] and MicroMegas [13]. For future SLHC upgrade, one of the most challenging objectives is realization of large area MPGDs.

2.1 Micromegas

Micromegas (MICROMEsh GAseous Structure) is a gaseous detector that has been developed initially for tracking in high rate high-energy experiments. At present, Micromegas detector is used in many experiments [14,15] and due to its high performances is being employed for searching rare events such as the Solar axion CAST [16] and also for neutron detection [17,18]. The Micromegas detector provides excellent position resolution and high counting rate performance, which can be combined with trigger capabilities. The Micromegas technology provides the possibility to produce mechanically robust large-size detectors with cost-effective industrial processes. The effort aims to improve the performance, the efficiency and the robustness of Micromegas based detectors. Thus, the Micromegas detector which is illustrated in Figure 2.1 is a promising candidate for the upgrade of the ATLAS Muon Spectrometer at the SLHC [19].

(a) **(b)** **(c)**

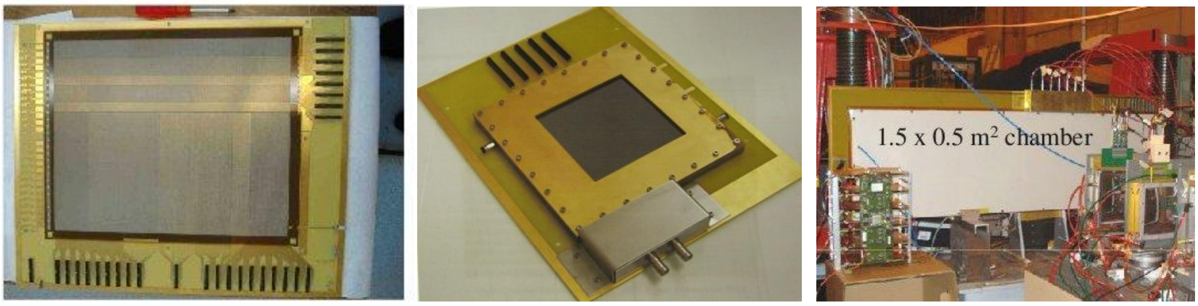

Figure 2.1 : (a) The first MAMMA Micromegas prototype (b) Microbulk 10x10cm^2 Micromegas (c) 50x150 cm^2 Micromegas detector

There are important requirements on Micromegas detector for the upgrade. For example, spatial resolution bigger than 100 μm which means the capability of a detector to separate the signals arising from two particles traversing the detector at close distance. Time resolution is about 5 ns which is the criterion for the quality of a time measurement. Efficiency is bigger than 99% which means the percentage of ionizing radiation hitting the detector that is measured and it is the ratio between the observed counts and the expected counts. Rate capability is bigger than 15 kHz/cm^2 (includes 200 Hz/cm^2 from neutron induced hits with E_n>100 keV). The detectors also have good double track resolution, and they can combine triggering and tracking functions together.

2.1.1 The principle of operation of the Micromegas

The principle of operation of the Micromegas detector is similar in other gaseous radiation detectors: radiation generates primary ionization in the gas by creating ionization path and releasing the electrons from the gas molecule, than primary electrons create further electron-ion pairs in an avalanche process in a region where a strong electric field is present [20]. The particles which are amplified and reach to the pad or the strip readout at the anode give the signal. The principle of operation of the Micromegas is shown in Figure 2.2. According to the figure, the distance between the drift electrode and micromesh is almost 5 mm and the distance between the micromesh and strips is 128 μm. It can be called as drift region and transfer region respectively. Primary electrons are created in the drift region, and the amplification of the electrons are generated in the transfer region.

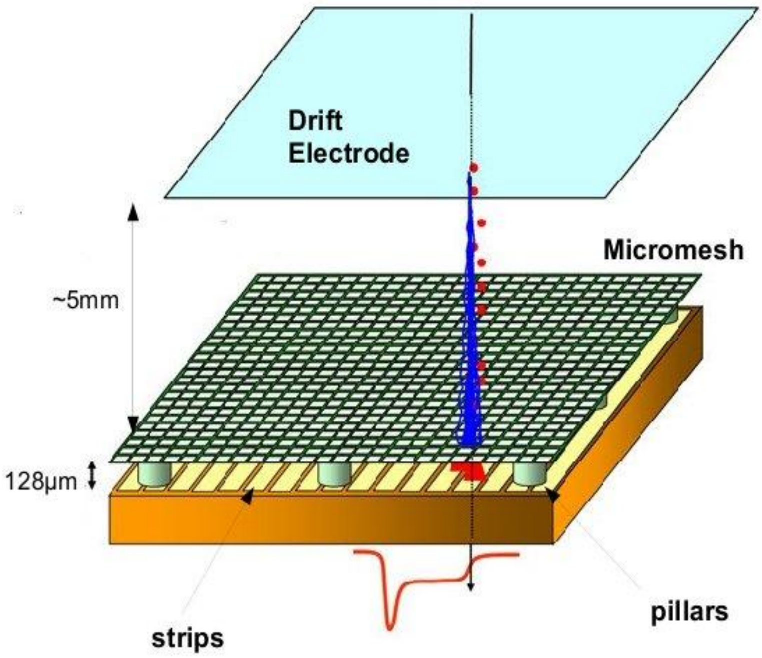

Figure 2.2 : The principle of the operation of the Micromegas detector

The Micromegas technology consists of an asymmetric two-stage parallel- plate gas detector. The first stage, about 5 mm thick conversion gap, is separated from the 128 μm thick amplification gap, by a micro-mesh foil resting on insulating spacers. The amplification gap is closed at the bottom by the pad anode surface. Such a configuration allows to establish simultaneously a very high electric field in the amplification region together with a low electric field in the drift region, by applying suitable voltages between the three electrodes (cathode-mesh-anode). When a charged particle traverses the conversion gap, it generates primary electrons which are subsequently multiplied in the small amplification gap. The associated ion cloud is quickly collected on the mesh layer generating a relatively fast signal, whereas only a small part of the ion cloud penetrates into the conversion region. The amplified electron cloud is collected on the anode providing a fast electric signal.

2.2 GEM

The Gas Electron Multiplier (GEM) is a proven amplification technique for position detection of ionizing radiation such as charged particles, photons, X-rays and neutrons, in gas detectors [21]. The GEM technology, which has been introduced by F. Sauli in 1996 is in use in high energy physics and medical physics.

The standard CERN-GEM detectors consist of an insulator made of a thin kapton foil (about 50 μm) which is coated on both sides with copper layers (about 5 μm). This structure is perforated with holes that typically have a diameter of 70 μm and a pitch of 140 μm. The holes are arranged in a hexagonal pattern. Due to an etching production process they have a double conical shape with an inner diameter of about 55 μm. Besides the CERN-GEM detectors, also other companies are now producing GEM foils, that vary in hole size, shape as well as the insulator thickness and material. Figure 2.3 shows an image of a GEM that has been taken with an electron microscope [22].

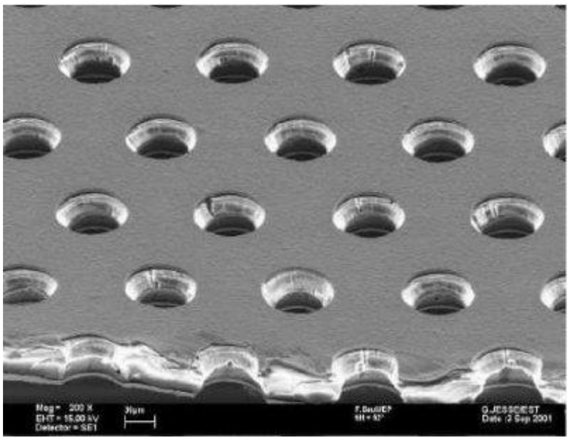

Figure 2.3 : The image of the GEM structure taken with an electron microscope

2.2.1 The principle of operation of the GEM

The operation principle of the GEMs is shown in Figure 2.4. Between the two copper coatings, a voltage of a few 100 V is applied. Since the electric field lines are focused in the holes, there the resulting electric field strength is in the order of some 10 kV/cm which is high enough for the gas amplification. It is possible to achieve an amplification up to ten thousand, but usually a setup consists of two or three successive GEMs which are operated at a lower voltage and therefore run more stable. Most electric field lines end on the side towards the cathode while on the other side most lines go into the direction of the anode. The ions from the gas amplification are pulled to and collected on the GEM surface while most of the electrons are extracted out of the GEM holes. The electron extraction is intensified if additionally magnetic field is applied perpendicular to the GEM plane.

The electrons tend to follow the magnetic field lines. The intrinsic ion back drift suppression is one of the main advantages of the GEM and cause making gating grid unnecessary. Another advantage of the GEM amplification is the fast signal: the electron signal is measured directly on the pad plane, which leads to a better time resolution. Furthermore, the GEM detectors can require less mounting structures as proportional wires can [23].

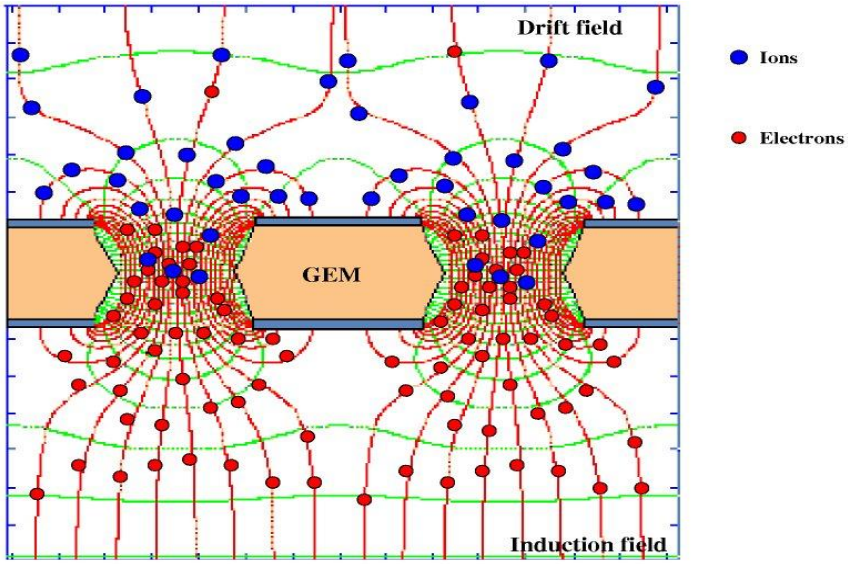

Figure 2.4 : The principle of the operation of GEM

The advantages of the GEM can be sorted as very high radiation rate capability, safe non-explosive gas mixtures, high sturdiness and reliability. GEM has flexible detector shape and readout patterns, and also high time and position resolutions, high performance at low cost. GEM can reach 1 MHz/mm^2 of photon flux rate, it has 40 μm of spatial resolution, almost 15-20% energy resolution, and 90% achievable gain. GEM detectors has also been applied successfully in other fields of research. For example, it is used for medical imaging for detection and treatment. GEM detectors are also susceptible to use for astrophysics, optical imaging of complex events, and dosimetry.

3. MEASUREMENTS AND PERFORMANCE TEST OF MICROPATTERN GAS DETECTORS

In this chapter, the measurements and performenace tests of the Micromegas and GEM are included. The test beam is also explained and it's emphasized the data analysis of the Micromegas.

3.1 Measurements and performance tests of Micromegas

Micromegas detector which is used in the laboratory tests is microbulk 10 cm x 10 cm detector with readout. The total size of the Micromegas detector is 325 mm x 250 mm x 35 mm.

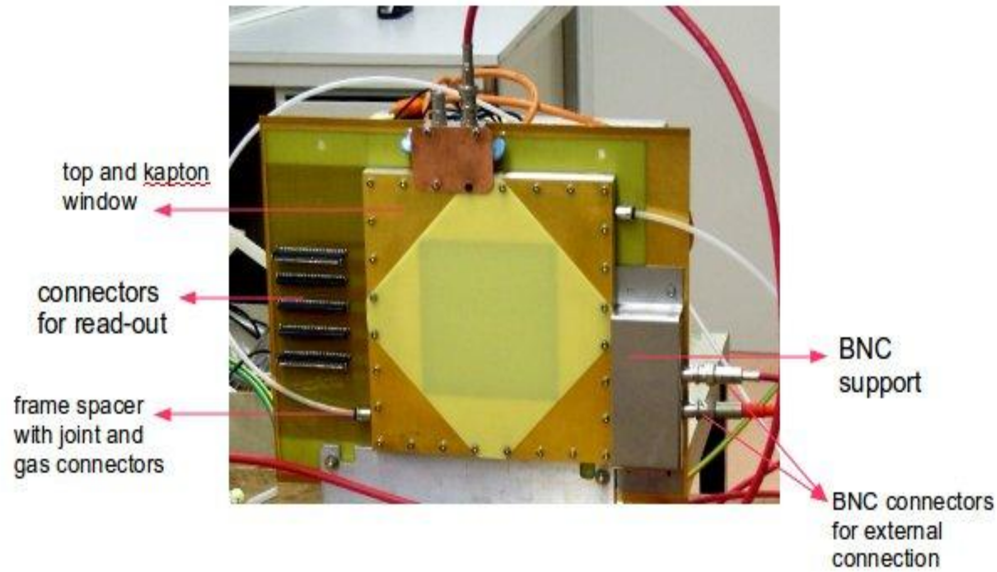

Figure 3.1 : External view of the Micromegas detector

In Figure 3.1 the external parts of the detector are shown. BNC (Bayonet Neill-Concelman connector) is a very common type of RF connector used for terminating coaxial cable. BNC connectors are used to connect the HV cables which do the internal electrical connections. There are two gas connections as input and output. There is a top epoxy (Ni/Au only on top) with kapton 10 cm x10 cm window. Above the kapton window there is a plastic support for the source. The internal connections are drift electrode, mesh and anode electrode which are shown in the Figure 3.2.

(a) **(b)**

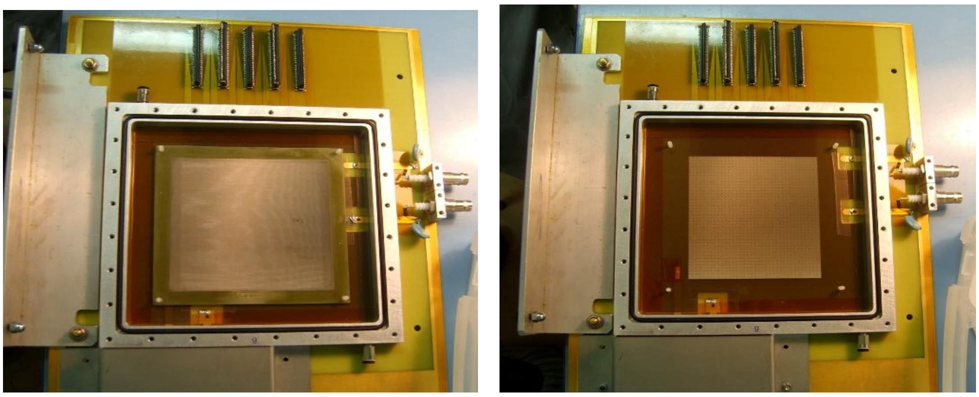

Figure 3.2 : (a) The view of the drift electrode (b) The view of mesh

Table 3.1 The specifications of Micromegas

Specifications	Values
Mesh pitch (μm)	45
Mesh wire diameter (μm)	18
Grid dimension (cm^2)	9x10
Coverlay dimension (cm^2)	14,7x14,7
Pillar diameter (μm)	300

The pillars are used to create pitch between mesh and drift, and to have the distance stable. The distance between mesh and drift is obtained using a spacer, so it is possible to change the width of the conversion gap. The distance was 7.2 mm for the gain measurement. The gas mixture was Ar(85%):CO_2(15%). The drift voltage is fixed as 700 V. The specifications for the measurement are shown in Table 3.2.

Table 3.2 The specifications of the gain measurement

Specifications	Values
Drift voltage (V)	700
Maximum mesh voltage (V)	585
Minimum mesh voltage (V)	500
Gas mixture	Ar: CO_2 (85:15)
Source	$_{55}$Fe

The aim was both to determine the electric field and the gain that is the ratio between the primary electrons and the electrons which reach the strips. The charge sensitive amplifier was used and the calibration input capacitance was 1,8 pF. Depending on the gas mixture composition and required gas gain, the value of the mesh voltage changes in from ~400 to ~600 V. For the gain measurement, the maximum value of the mesh voltage was 585 V because of the spark problem. Imperfections of the detector or unusually large energy losses can cause discharges. Gain above a few thousand and discharges can damage the strips in the detector or produce a short circuit in the worst case. These effects cause very high increase of the spark probability and prevent to reach to higher voltages. Therefore, careful choice of the gas mixture and the materials used in the micro strip gas chambers could lower the effects. The noble gases like Argon, Helium and the quencher gases like CO_2, CF_4 can be mixed. The avalanche multiplication happens at much lower fileds so noble gases used for the main component of the gas mixture and called as counting gases. Besides, pure noble gases make the detector too vulnerable for discharges, so the quencher gases are added.

The amplitude of the output signal from the ^{55}Fe source could be calculated for the gas gain of 10^4 as an example. The total number of the ionization electrons for 4-7 mm of drift space is about two orders of magnitude. For the gas gain, $G_{GAS}=10^4$ the total charge Q of the signal is written like in the equation **(3.1)**.

$$Q = N_e.Q_e.G_{GAS} = 1,6.10^{-13}C \quad \textbf{(3.1)}$$

where Q_e is $1,6.10^{-19}$ C and N_e is the number of the ionization electrons.

The circuit diagram of the input part of the charge sensitive pre-amplifier and also the calibration input are shown in Figure 3.3.

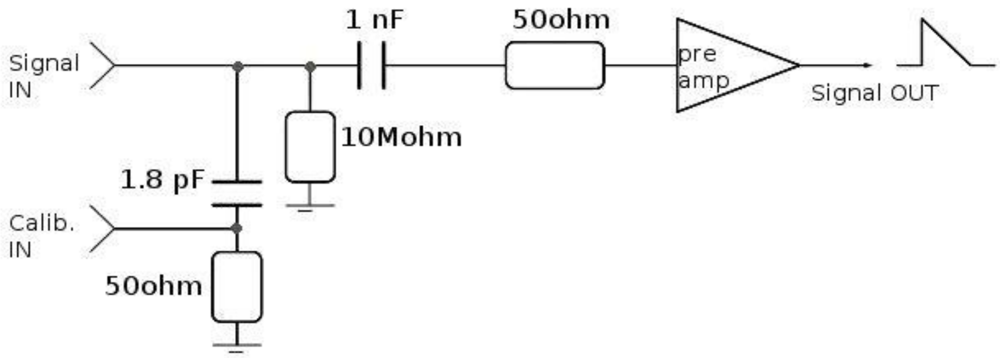

Figure 3.3 : The charge sensitive pre-amplifier

The input capacitance of the pre-amplifier is ~750 pF. The charge flows to the charge sensitive pre-amplifier input RC chain with the integration time is shown in the equation **(3.2)** .

$$\tau = RC = 750.10^{-12}.50 = 37.5ns \quad \textbf{(3.2)}$$

where R is the value of the resistor and C is the value of the capacitor.

The current is calculated with the equation **(3.3)** ,so the amplitude of the signal V is 0.2 mV respectively.

$$I = \frac{Q}{\tau} = \frac{1{,}6.10^{-13}}{37{,}5.10^{-9}} = 4\mu A \qquad \textbf{(3.3)}$$

From the direct calculation with the equation **(3.4)** the amplitude of the signal can be found.

$$V = \frac{Q}{C} = \frac{1{,}6.10^{-13}}{750.10^{-12}} = 0{,}2mV \qquad \textbf{(3.4)}$$

To simulate the input charge of $Q=1{,}6.10^{-13}$ C from ^{55}Fe source, the amplitude of the pulse at the calibration input must be equal to the equation **(3.5)** .

$$V = \frac{Q}{C} = \frac{1{,}6.10^{-13}}{1{,}8.10^{-12}} = 90mV \qquad \textbf{(3.2)}$$

Therefore, when the amplitude of the calibration pulse is 90 mV, the output signal from the pre-amplifier corresponds to the ^{55}Fe signal from the Micromegas chamber with the gas gain of 10^4.

To calculate the gain for the measurement which the specifications are shown in Table 3.2, the number of the primary electrons is calculated from the equation **(3.6)**.

$$n_{primary} = \frac{E_\gamma}{W_i} \qquad \textbf{(3.6)}$$

where $E\gamma$ is the energy of the photons, 5.9 keV for ^{55}Fe, and W_i is the ionization energy of the gas which is 26 eV for Ar (85%) and 33 eV for CO_2 (15%) is about 220.

The number of the total electrons is the sum of the primary electrons and produced electrons in avalanche, and it's given as the equation **(3.7)**.

$$n_{total} = \frac{C.V}{Q_e.K} \qquad \textbf{(3.7)}$$

where C is the capacitance (1,8 pF), V is the pulse height (0,2 V), K is the calibration factor (5,28) of the electronics and Q_e is the charge of electron.

The total number of electrons, n_{total} is approximately 10^6. Gain, G is the ratio between n_{total} and $n_{primary}$ which is shown in the equation **(3.8)**.

$$G = \frac{n_{total}}{n_{primary}} \tag{3.8}$$

Consequently, the gas gain is about 10^4.

In Figure 3.4, gas gain for various electric fields is shown, and the maximum gain is approximately 10^4.

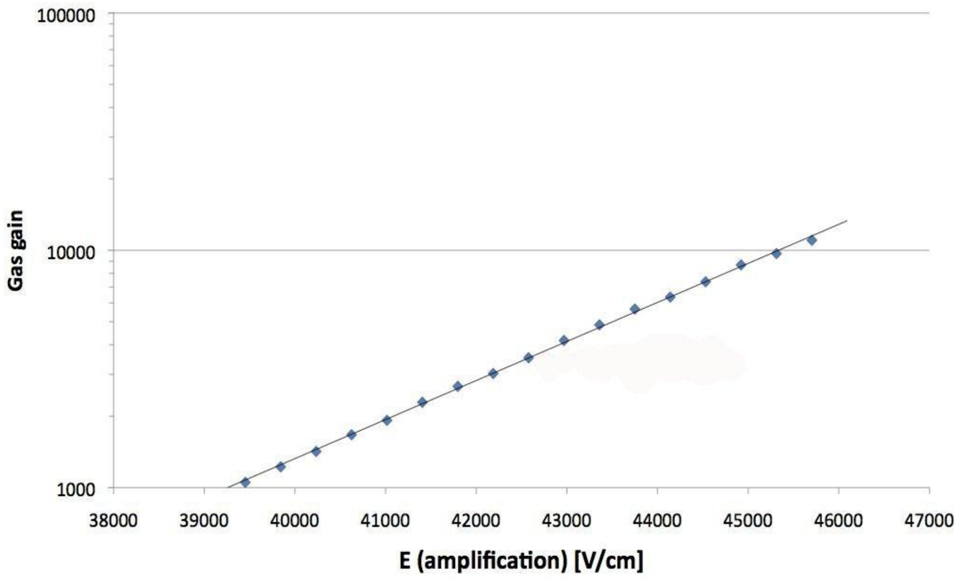

Figure 3.4 : Gas gain for different electric fields (amplification gap is 0,128mm)

Afterwards, the V_M was fixed to identify the ratio between the electric fields of the amplification gap and the conversion gap by changing the V_D. Therefore, the electric field of the amplification gap was fixed, and the electric potential of the conversion gap rose with the increasing of the V_D .The distance between mesh and drift electrode was 4,2 mm, and the conditions during the ratio measurement are shown in Table 3.3.

Table 3.3 The specifications of the ratio measurement.

Specifications	Values
Mesh voltage (V)	540
Maximum drift voltage (V)	3800
Minimum drfit voltage (V)	600
Gas mixture	Ar: CO_2(85:15)
Source	$_{55}$Fe

If the maximum signal amplitude is accepted as 100%, the plot of ratio between the electric field of amplification gap and drift gap, E_{amp} / E_{drift} becomes as in Figure 3.5.

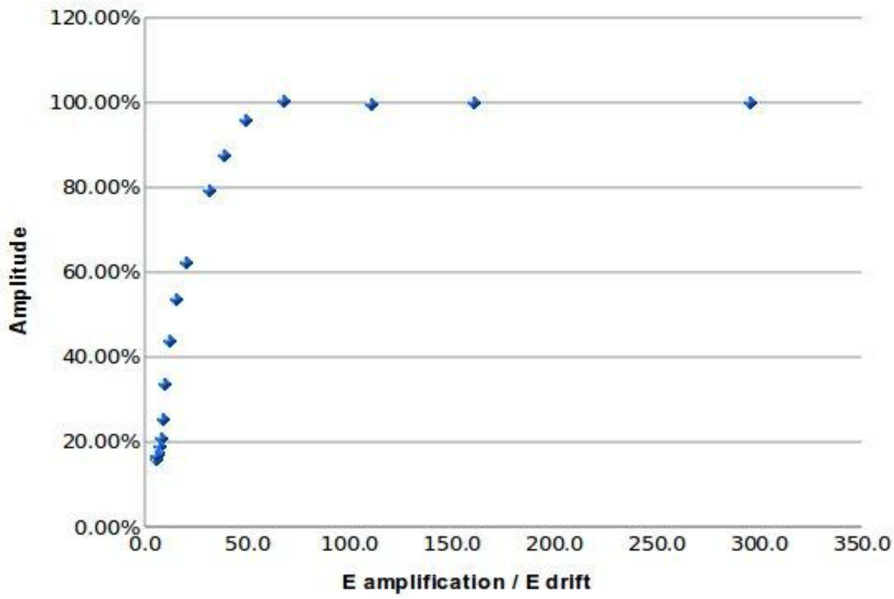

Figure 3.5 : The ratio between electric fields of amplification gap and conversion gap

When the electric field in the amplification region becomes too large compared to the one in the drift field region, the signal amplitude does not change anymore because of the transparency of the mesh. Electrical transparency is the ratio of the charge reaching the amplification region to the total charge arriving at the pad or mesh. Figure 3.5 shows that the transparency of the mesh becomes maximum at E_{amp} / E_{drift} is about 70.

3.1.1 The spectrum of ^{55}Fe

The typical spectrum of ^{55}Fe taken with Micromegas is shown in Figure 3.6. The first peak is escape peak and the second peak is the main peak. The main peak is due to the full energy deposition of the 5,9 keV gamma line of ^{55}Fe source. However, escape peak is due to the non-full energy deposition of the 5,9 keV gamma line of the source in the detector. If the energy of incident photon exceeds binding energy of the electrons in the shell, the photon is completely absorbed. The secondary photon with an energy just below the shell has a very long absorbtion length, therefore can escape the volume of detection, and this creates the characteristic escape peak of the gas. The peak position is also proportional to the energy of the source in an energy spectrum.

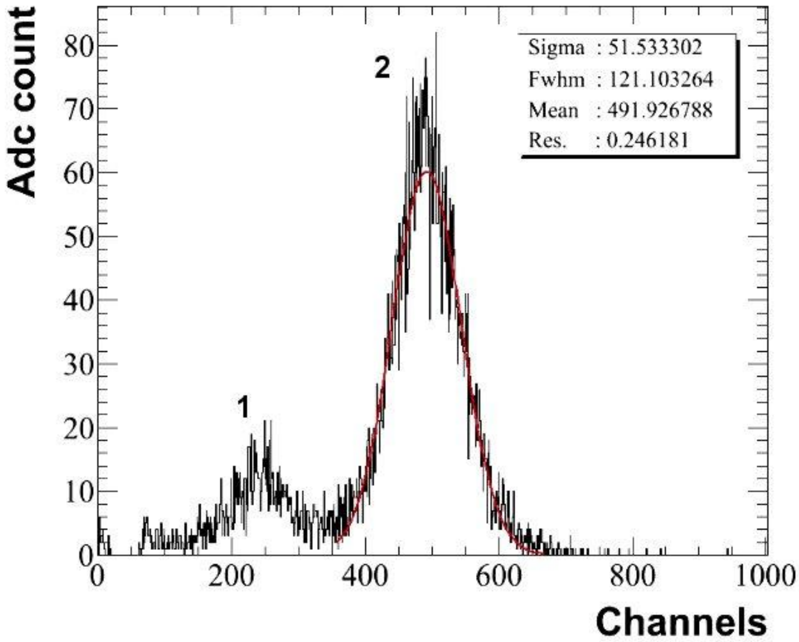

Figure 3.6 : Spectrum collected from an ^{55}Fe radioactive source

According to Figure 3.6, the standard deviation, σ is about 51,5. FWHM (Full Width at Half Maximum) is calculated as in the equation **(3.9)**.

$$FWHM = \sigma.2{,}35 = 121{,}1 \quad \textbf{(3.9)}$$

The most common figure used to express detector resolution is FWHM. The resolution is inversely proportional with FWHM. This means, the smaller FWHM is the better resolution. The equation **(3.10)** shows the calculation of the resolution.

$$\%resolution = \frac{FWHM}{mean}.100 = \%24{,}6 \quad \textbf{(3.10)}$$

where mean is the middle of the peak which is fitted and shown with red line.

3.2 Measurements and performance tests of Micromegas + GEM

The GEM foil was submitted into the Micromegas detector for preamplification. The aim of the two-stage amplification structure is to reduce the spark probability on a Micromegas detector, so the gain is splitted in two stages. Higher voltages cause the spark and with more than one stage, the gain can be increased using lower voltages.

The distance between drift electrode and GEM was 3,25 mm, and the distance between GEM and mesh was 2,2 mm for the measurements. GEM can have very different kinds of geometries, in this part it has hexagonal hole geometry,and also the biconical holes. The connection of GEM to the MM is shown in Figure 3.7. The standard GEM foil was used,and the specifications of GEM are shown in Table 3.4.

Table 3.4 : The specifications of GEM

Specifications	Values
Hole pitch (μm)	140
Hole outer diameter (μm)	70
Inner diameter (μm)	50
Kapton thickness (μm)	50
Copper thickness (μm)	5

(a) **(b)**

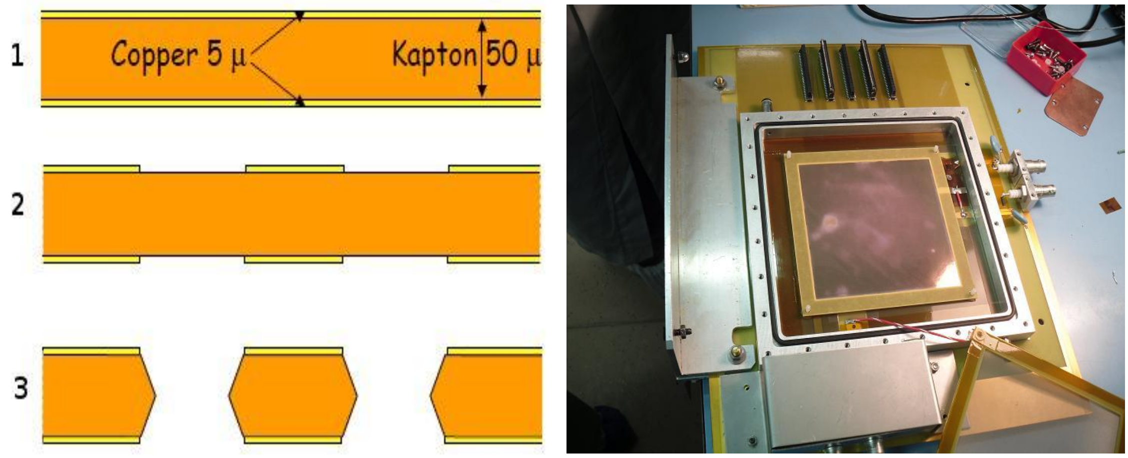

Figure 3.7 : (a) From number 1 to 3, GEM foil with the etching production process has a double conical shape (b) connection of GEM to the MM

The voltage scans which are mentioned in the section 3.2.2 were made with Micromegas + GEM detector to understand the characteristics of the detector better. The gas mixture was Ar (90%) : CF_4 (10%) ,and flow rate was about 10 litre/hour. The block diagram of the test bench is shown in Figure 3.8.

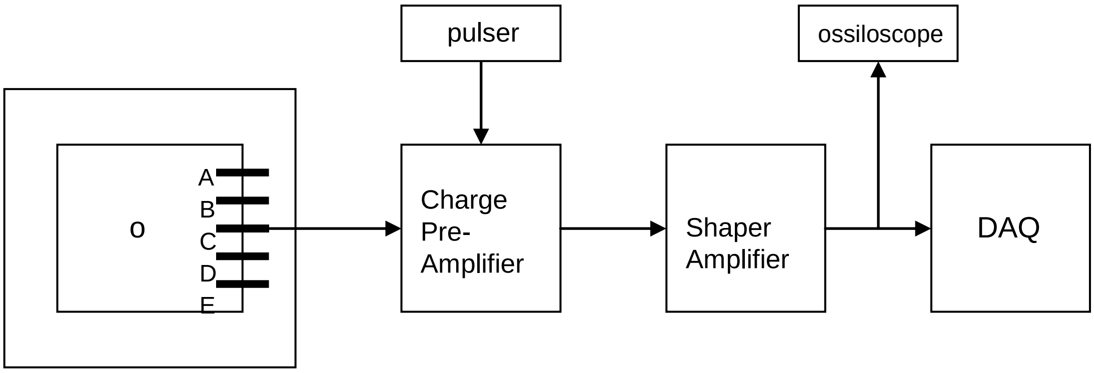

Figure 3.8 : Block diagram of the test bench

The Micromegas is connected to the charge pre-amplifier with its readout system to deposit the total charges then it connects to the shaper amplifier, and DAQ is connected to the shaper amplifier according to the Figure 3.8.

3.2.1 The X-ray Setup

The X-ray setup was used to measure the calibrated gain, also calculate the resolution, the spark probability using alpha particles from Th source, and get the current. ^{55}Fe and X-ray source were used on the Micromegas, and two spectra were taken from both ^{55}Fe and X-ray source. In Figure 3.9, the X-ray setup is shown with the Micromegas. The specifications for the measurement are given in Table 3.5.

(a) **(b)**

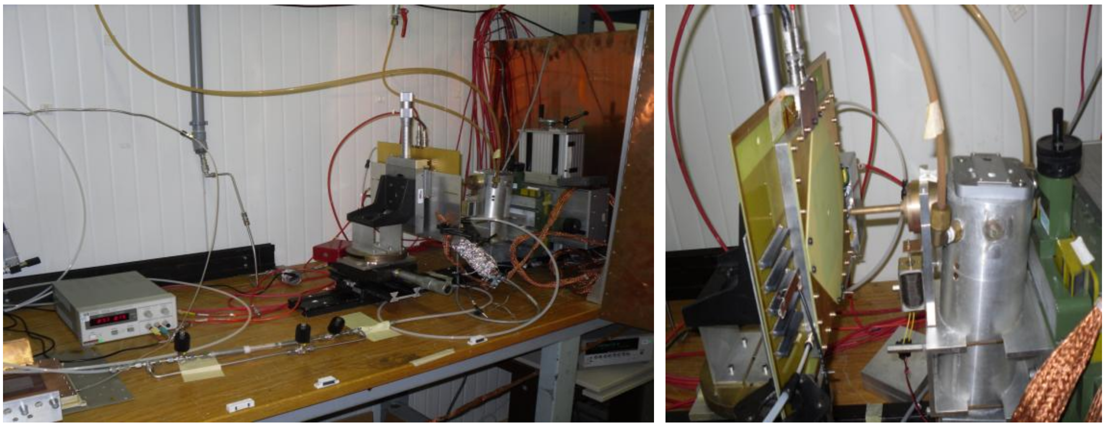

Figure 3.9 : (a) The complete X-ray setup (b) Micromegas detector.

Table 3.5 : The specifications of X-ray measurement

Specifications	Values
V_D (V)	1125
V_{GT} (V)	925
V_{GB} (V)	600
V_M (V)	500
Gas	Ar:CF_4 (90:10)
Drift field (kV/cm)	0.615
Transfer field (kV/cm)	0.455

The spectra of the ^{55}Fe and the X-ray source is shown in Figure 3.10, and there are 4 peaks as pedestal, main peak, escape peak, and peak of conversion of X-ray and ^{55}Fe in the transfer region. Pedestal is the background that the electronic equipments cause, because there are no electronic components that behave ideally in real world. Therefore, the available electronics have noise level for the detector. The escape peak from the transfer region is not seen since it is too small.

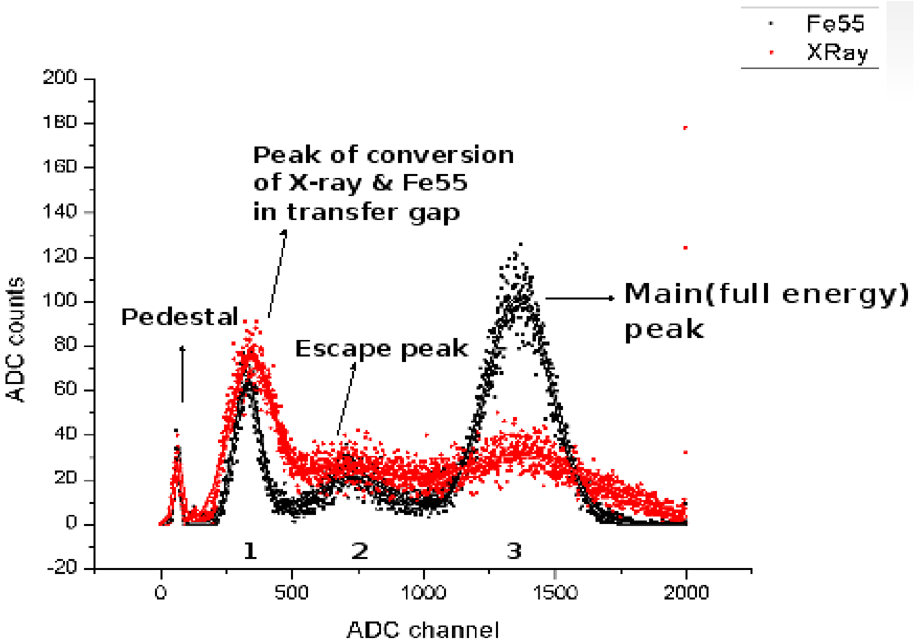

Figure 3.10 : The spectra of the ^{55}Fe and the X-ray source

For the ^{55}Fe spectrum the specifications are shown in Table 3.6.

Table 3.6 : The analysis of ^{55}Fe spectrum

Peak	Area	Center	Width	Height
1	7525.5	329.44	94.303	63.673
2	9003.9	740.75	344.87	20.832
3	32129	1362.1	250.03	102.53

For the X-ray spectrum the specifications are shown in Table 3.7.

Table 3.7 : The analysis of the the X-ray spectrum of the X-ray source

Peak	Area	Center	Width	Height
1	14312	343.49	160.95	70.950
2	11063	667.66	365.57	24.146
3	23989	1356.1	623.26	30.710

The count rate was determined for three current values. These values are; high current with the attenuator(C1), low current with attenuator(C2), and low current without the attenuator(C3). Count rate measurements were repeated five times for each case, and the average value of them was determined. After the subtraction of the noise, the counts were 6385, 359 and 159070 respectively. However, the count rate due to the high current value (11.7 nA) without attenuator was used for the calculation of the gain, because good precision was wanted on the measurement, so high current was needed. Since aim was to find the average gain of the amplification, three consecutive below, peaks of the spectrum were used. The current was calculated with the equation **(3.11)**.

$$I = \frac{\Delta Q}{\Delta t} = \frac{G.p_{\gamma}.Q_e.counts}{\Delta t} = \frac{G.160.Q_e.C1.C3}{\Delta t.C2} \quad \textbf{(3.11)}$$

where G is the number of electrons generated by 5.9 keV photon in gas, Q_e is the electron charge and p_γ is the number of primaries (160). According to the equation **(3.11)**, the gain can be written such the equation **(3.12)**.

$$gain = \frac{I.C2.\Delta t}{160.C1.C3.Q_e} \cdot \frac{\dfrac{\sum_{i=2}^{3} E_i.A_i}{\sum_{i=2}^{3} A_i}}{\dfrac{\sum_{i=1}^{3} E_i.A_i}{\sum_{i=1}^{3} A_i}} \quad \textbf{(3.12)}$$

where E is the area, A is the center of the peaks, C1,C2,C3 are the counts, Δt is the time(10), Q_e is the electron charge. (C1.C3)/C2 in the equation **(3.11)** refers to the rate with high photon intensity without an absorber. To quantify the gain, values in the Table 3.10 and 3.11 were used in the equation (**3.12a)**.

$$gain = \left(\frac{11{,}7.10^{-9}.359.10}{160.6385.159070.1{,}6.10^{-19}}\right) X \left(\frac{\dfrac{(11063.667{,}66)+(23989.1356{,}1)}{11063+23989}}{\dfrac{(14312.343{,}49)+(11063.667{,}66)+(23989.1356{,}1)}{14312+11063+23989}}\right)$$

(3.12a)

The calculated gain (calibration of the charge sensitive pre-amplifier) was turned out to be 1473 with the equation (**3.12a)**.

3.2.2 Voltage Scans

In order to understand voltage-gain relation of the detector, a serious of voltage scans were performed. The optimum values of the voltages and electric fields were determined by changing the voltages according to the scans.

3.2.2.1 GEM Voltage Scan

For GEM voltage scan, mesh voltage V_M and GEM bottom voltage V_{GB} were fixed to the value of 500 V and 600 V respectively. Table 3.8 shows the affect of drift voltageV_D and GEM top voltage V_{GT} voltages to the overall gain.

Table 3.8 GEM voltage scan of MM+GEM

Drift (V)	GEM_{top} (V)	ΔV_{GEM} (V)	Amplitude (V)	Gain
800	600	0	0,430	323
825	625	25	0,431	323
850	650	50	0,439	329
875	675	75	0,429	322
900	700	100	0,422	317
925	725	125	0,421	316
950	750	150	0,423	317
975	775	175	0,440	330
1000	800	200	0,444	333
1025	825	225	0,386	290
1050	850	250	0,576	432
1075	875	275	0,865	649
1100	900	300	1,135	851
1125	925	325	1,964	1473
1150	950	350	3,330	2498
1175	975	375	5,370	4028
1200	1000	400	9,280	6960
1210	1010	410	10,750	8063

The electric field of the conversion gap which is also called as drift field was 0,62 kV/cm, and the electric field of the amplification gap which is also called as transfer field was 0,45 kV/cm. Figure 3.11 shows the gain vs ΔV_{GEM} ,and the increasing gas gain starts after ΔV_{GEM} reaches to 225 V. When the voltage of the GEM wasn't large enough, its transparency was started to decrease, and the signal became smaller. The ideal ΔV_{GEM} was chosen as 325 V for the next scans, and the voltages were increased according to this initial value.

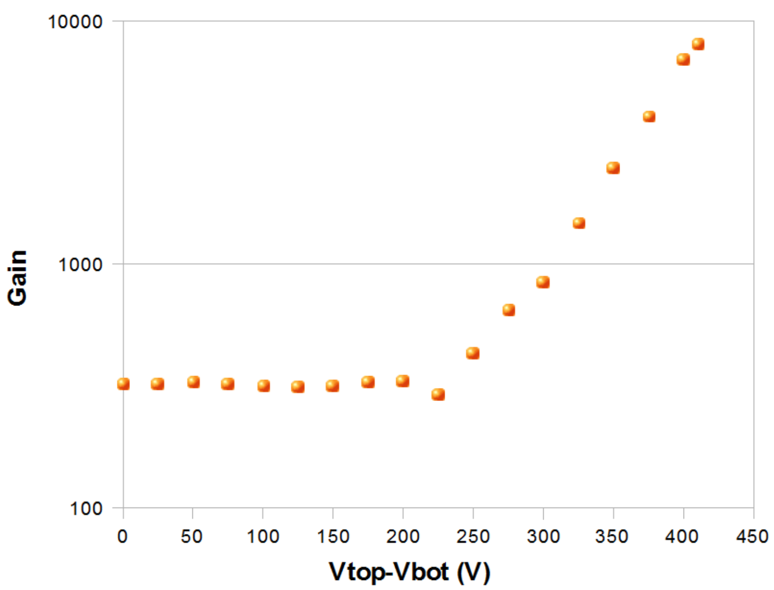

Figure 3.11 : GEM voltage scan

3.2.2.2 Mesh Voltage Scan

For mesh voltage scan, V_M was changed together with the other voltages as shown in Table 3.9.

Table 3.9 : Mesh voltage scan of MM+GEM

Drift (V)	GEM_{top} (V)	GEM_{bot} (V)	Mesh (V)	Amplitude (V)	Gain
1025	825	500	400	0,144	108
1045	845	520	420	0,201	151
1065	865	540	440	0,311	233
1085	885	560	460	0,495	371
1105	905	580	480	0,886	665
1125	925	600	500	1,431	1073
1145	945	620	520	2,700	2025
1165	965	640	540	5,380	4035
1185	985	660	560	16,66	12495
1195	995	670	570	25,00	18750

The electric field of the conversion gap was 0,62 kV/cm, and the electric field of the amplification gap was 0,45 kV/cm. The electrons which are amplified two times with the electric field of the mesh and GEM by increasing all voltages are determined.

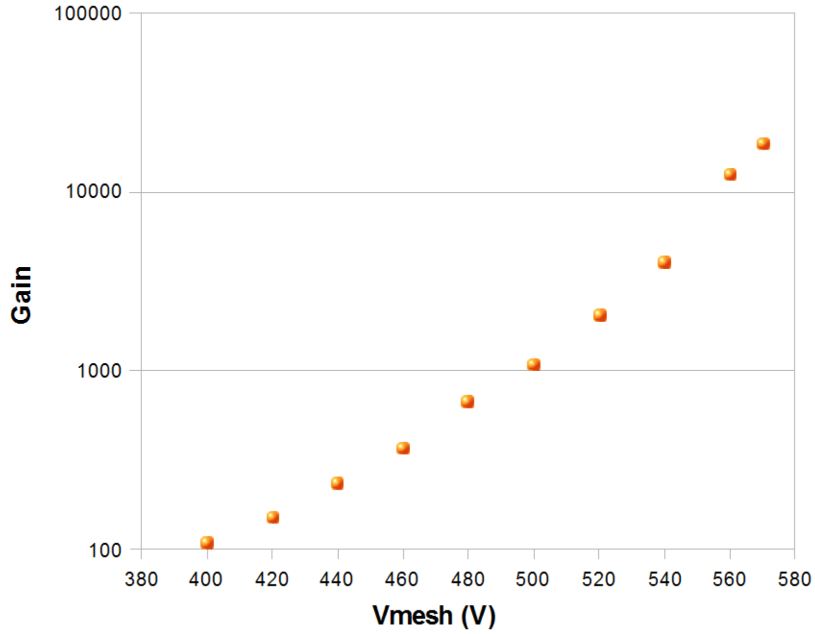

Figure 3.12 : Mesh voltage scan

The electrons get through the amplification gap faster at higher voltages and as a result more electrons reach to the strips. It means that gas gain increases because of the rising number of electrons. Figure 3.12 shows rising gain corresponding to V_M.

3.2.2.3 Transfer field scan

The effect of the electric field between GEM and mesh in the detector was examined with the transfer field scan. For transfer field scan V_M was fixed to the value of 500 V, and the other voltages were changed, so the electric field between anode electrode and mesh was fixed. Table 3.10 shows the voltage scan of the MM+GEM detector.

Table 3.10 : Transfer field scan of MM+GEM

Drift (V)	GEM $_{top}$ (V)	GEM $_{bot}$(V)	E_t (kV/cm)	Amplitude (V)	Gain
1135	935	610	0,50	1,566	1175
1190	990	665	0,75	2,110	1583
1245	1045	720	1,00	2,330	1748
1300	1100	775	1,25	2,470	1853
1355	1155	830	1,50	2,450	1838
1410	1210	885	1,75	2,340	1755
1465	1265	940	2,00	1,865	1399
1520	1320	995	2,25	1,447	1085
1575	1375	1050	2,50	0,984	738

The distance between mesh and GEM was 2,2 mm. The potential difference between V_{GB} and V_M was 110 V corresponds to 0,5 kV/cm transfer field. Knowing the optimum ΔV_{GEM} was 325 V, V_{GT} was increased gradually by holding ΔV_{GEM} fixed. The drift field was 0,62 kV/cm.

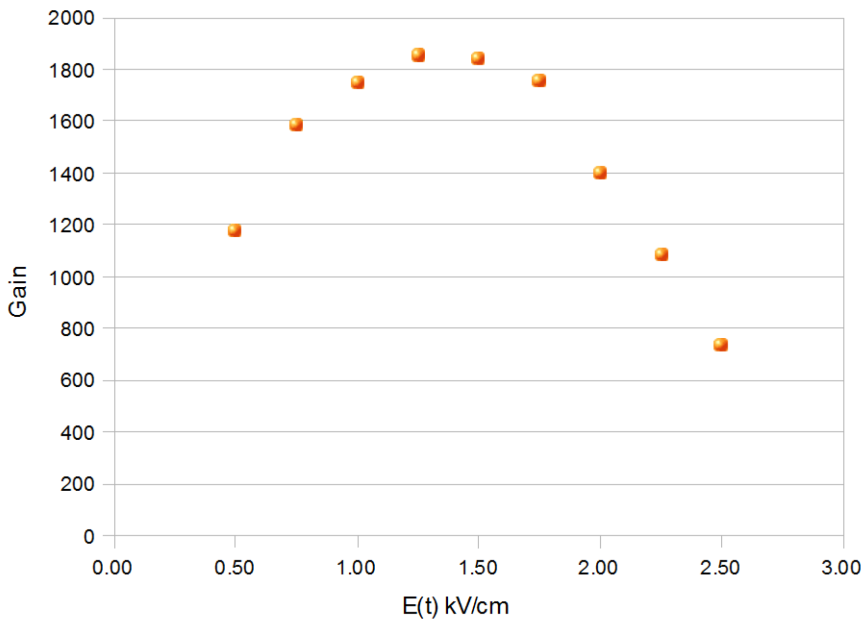

Figure 3.13 : Transfer field scan

When the electric field between mesh and GEM is very low, the electrons are not efficiently extracted from the GEM. At very high transfer fields the transparency of the mesh is also very low. Therefore, the optimum value for the transfer field is at 1,25 kV/cm as seen in Figure 3.13.

3.2.2.4 Drift Field Scan

For drift field scan V_M , V_{GB}, and V_{GT} were fixed to the value of 500 V, 775 V and 1100 V respectively. The electric field of conversion gap was changed, so that the relation between drift field and gain could be determined. The transfer field was accepted as 1,25 kV/cm where this value was optimum for the measurement according to the transfer field scan. Since transfer field distance was 2,2 mm , the potential difference in the transfer field was 275 V. Therefore V_{GB} was 775 V. Table 3.11 shows the voltages for drift field scan.

Table 3.11 : Drift field scan of MM+GEM

Drift (V)	E(d) (kV/cm)	Amplitude (V)	Gain
1116	0,05	2,286	1715
1133	0,10	2,300	1725
1165	0,20	2,320	1740
1198	0,30	2,320	1740
1230	0,40	2,287	1715
1263	0,50	2,305	1729
1425	1,00	2,330	1748
1588	1,50	2,286	1715
1750	2,00	2,030	1523
1913	2,50	1,230	923

Figure 3.14 shows the transparency of GEM remains constant up to 1,5 kV/cm drift field, and then decreases rapidly as the drift field increases.

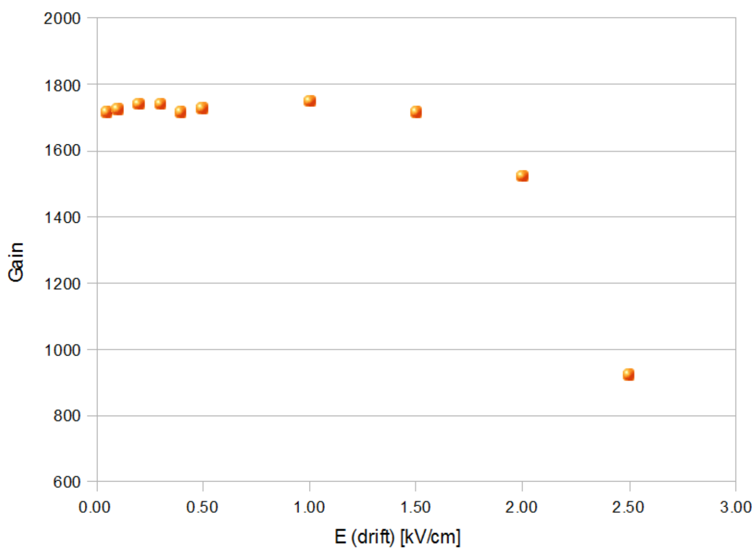

Figure 3.14 : Drift Field Scan

3.2.2.5 Mesh Voltage Scan (inverted GEM and drift)

The V_D and V_{GT} were inverted for this measurement. The aim was to determine the contribution of the transfer field and compare with the previous voltage scans. The mesh voltage scan is shown in Table 3.12.

Table 3.12 : Mesh voltage scan (inverted GEM and drift) of MM+GEM

Drift (V)	GEM $_{top}$ (V)	GEM $_{bot}$ (V)	Mesh (V)	Amplitude (V)	Gain
420	520	540	440	0,128	96
440	540	560	460	0,157	118
460	560	580	480	0,241	181
480	580	600	500	0,407	305
500	600	620	520	0,755	566
520	620	640	540	1,435	1076
540	640	660	560	3,640	2730
550	650	670	570	7,150	5363

In this case the drift field was -0,31 kV/cm, and transfer field was 0,45 kV/cm. The gain plot is shown for the inverted mesh voltage scan in Figure 3.15. This means the electrons are efficiently extracted from the mesh, so the gain increases with increasing of the mesh voltage.

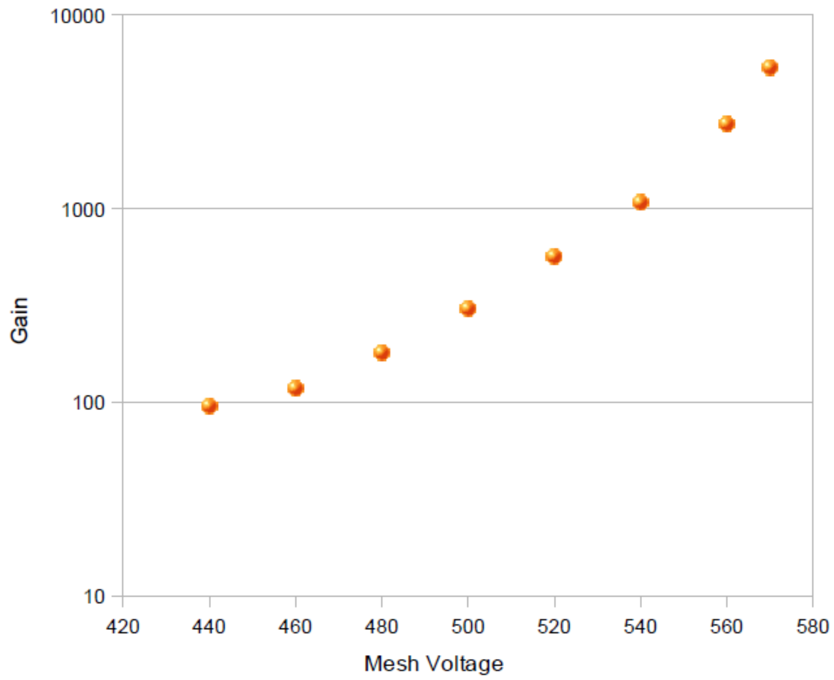

Figure 3.15 : Mesh Voltage Scan (inverted GEM and drift)

3.2.3 Resolution of MM + GEM detector

According to the conditions shown in Table 3.13, the resolution and gain were calculated with respect to the mesh voltage.

Table 3.13 : The specifications for the resolution and gain measurement

Specifications	Values
Drift field (kV/cm)	0,62
Transfer field (kV/cm)	1,25
GEM voltage (V)	325
Gas mixture	Ar:CF_4 (90:10)

The resolution and the gain are calculated step by step with the different voltages which are shown in Table 3.14.

Table 3.14 : The results with respect to different voltages for gain and resolution measurement

Drift (V)	GEM_{top}(V)	GEM_{bot}(V)	Mesh(V)	Gain
1125	925	600	500	1473
1200	1000	675	400	145
1220	1020	695	420	238
1240	1040	715	440	357
1260	1060	735	460	594
1280	1080	755	480	1048
1300	1100	775	500	1772
1320	1120	795	520	5538
1320	1120	795	520	5538
1340	1140	815	540	10839

According to the results in Table 3.14, the plot is shown as gain versus V_M and resolution versus V_M in the Figure 3.16. The gain reaches about 10^4, and the better resolution is about 21%. The energy resolution is calculated as the ratio between FWHM and mean of the each taken spectrum. According to the Table 3.14, the first row shows the calibrated gain value 1453. All other gain values are calculated by taking up 1453 as reference value. The calculation method of the gain is same with the voltage scans which are mentioned in the subtitles of 3.2.2. After division of the 1473 to its amplitude value, then it is multiplied with the amplitude of each high voltage value to find the gain.

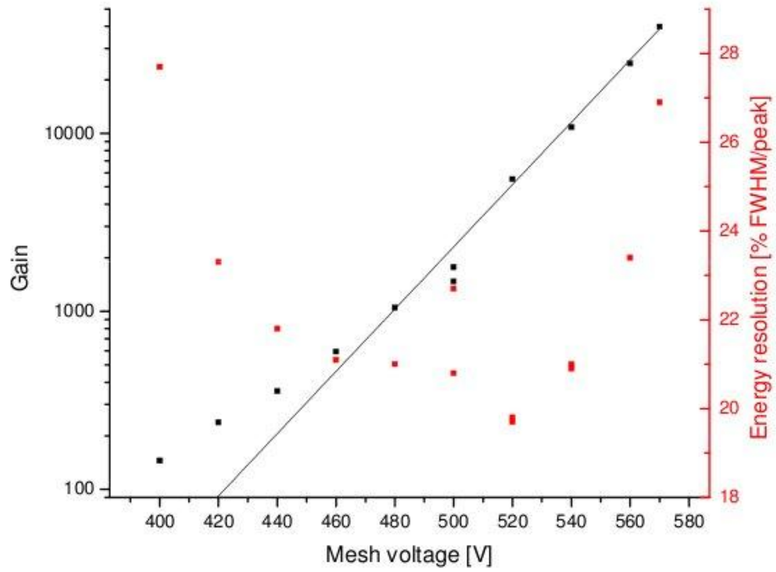

Figure 3.16 : Gain and resolution due to the voltage of mesh

3.2.4 The Spark measurement of MM + GEM detector

In order to study the spark probability, an alpha source Thorium was used. Since the specific ionization of α particles is larger compared to X-ray, and α particles create more ions in the detector. More ions mean more spark effect. For the spark measurement, the rate of alphas were measured. The gas was the Ar:CF_4(90:10) and the flow rate was 5 l/h. The conditions are shown in Table 3.15.

Table 3.15 : The parameters of the spark measurement

Parameters	Values
V_D (V)	1200
V_{GT} (V)	1000
V_{GB} (V)	675
V_M (V)	400
Drift field (kV/cm)	0.62
Transfer field (kV/cm)	1,25

With the increasing voltages, the rate of the alphas are also increased as it shown in the table 3.16. The alpha counts were made in every 10 seconds and the alpha rate is measured. The spark was observed after the mesh voltage reached to 485 V, also the drift voltage 1285 V and GEM voltage 325 V. On the other hand, the values of drift field and transfer field were chosen due to be enough for an efficient collection of charges produced in the drift space and transfer space.

Table 3.16 : The alpha rate due to the different voltages

Mesh [V]	GEM_{top} [V]	GEM_{bot} [V]	Drift [V]	Alpha rate (10 seconds)
400	675	1000	1200	124
410	685	1010	1210	135
420	695	1020	1220	133
430	705	1030	1230	145
440	715	1040	1240	149
450	725	1050	1250	158
460	735	1060	1260	162
470	745	1070	1270	171
480	755	1080	1280	190
485	760	1085	1285	215
490	765	1090	1290	224
495	770	1095	1295	239
500	775	1100	1300	248

For the last 4 measurements, the spark was observed in the different time intervals. In Table 3.17, the spark probability is shown for the alpha rates which were collected according to the voltages in Table 3.16. The Standard deviation is shown with Stdv and Δt spark is the time between one spark and the following spark in second according to the Table 3.17. The Standard deviation of the mean is calculated with the ratio of the Standard deviation and the square root of 10 seconds.

Table 3.17 : The spark probability due to the alpha rate

Alpha rate	Δt spark (s)	Stdv	Stdv of mean	Spark probability
215	80	101	32	6,3E-04
224	30	15	4,6	1,7E-03
239	12,3	11	3,4	4,1E-03
248	14,1	10	3,2	3,5E-03

Figure 3.17 shows the spark probability vs $V_{M.}$ When V_M increases with $V_{GT,}$ V_{GB} and V_D, the spark probability also increases. The spark effect prevents to reach higher voltages. To create more amplification gain, higher voltages are necessary. Moreover, origin of the sparks is due to the highly ionizing particles. These very large charges can only result from the secondary particles created in nuclear interactions of beam particles with gas or the walls of chamber. Spark probability produces a serious limitation when the detector has to deal with very high rate hadron flux.

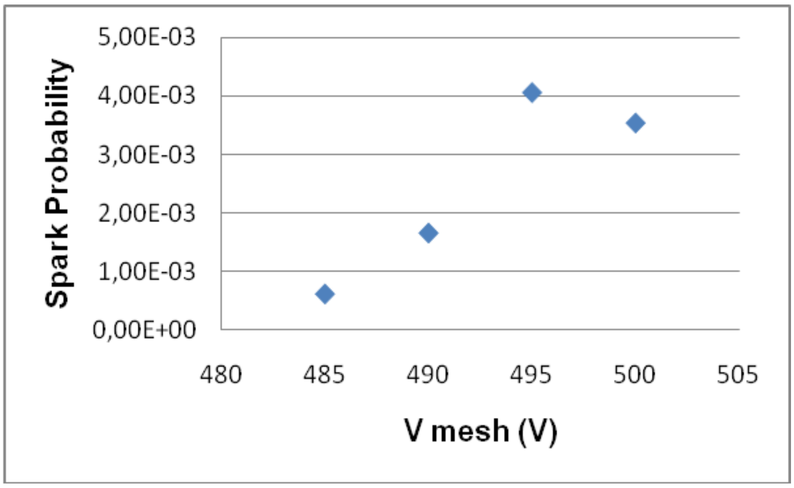

Figure : 3.17 : The plot of spark probability measurement

3.3 Test-Beam

The different kinds of prototypes of the Micromegas detectors have been performed periodically with the beam tests. The run conditions of some example runs from the test beam are shown in Figure 3.19. The **Run#** is the number of the run, **HV-M** is the high voltage of the mesh, **HV-D** is the high voltage of the drift, **Conn** is the strips which are connected, **Pitch** is the distance from the middle of one strip to the middle of the next strip, **Strip** is the strip width, **MM Evts** and **Si Evts** are the number of the events for the Micromegas and Silicon detectors respectively for the run. **Gas** shows the gas used, and **Chamber Name** defines the prototype being used during the run.
P1 is 350x450 mm^2 standard detector which has various strip pitches. It's a reference chamber for the test beams, and in Figure 3.22, the order of the strips is shown. **P3** is 500x1500 mm^2 standard detector which has 6 mesh segments and 250 - 500 μm strip pitches. The length of the strips are 400 and 1000mm, and it's shown in Figure 3.18.

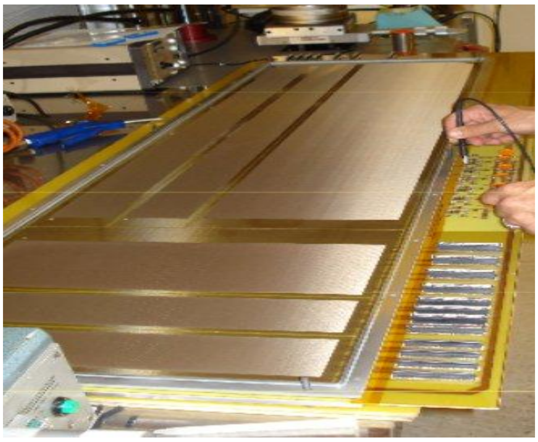

Figure 3.18 : P3 prototype of the Micromegas

S3 is the 100x100 mm^2 standard detector which has 250 µm strip pitch. **R3** detector is a kind of the S3 with resistive paste on the strips (with 150-200 µm thickness, 10 MΩ resistance), and covered with metallic pads with 1 mm x 0,15 mm dimensions. **R5** detector is also a kind of the S3 with resistive paste (with 1 mm thickness, 5 kΩ resistance) and it has metallic pads above the strips. MM(S2)+GEM/MM is used for double stage amplification which is mentioned in the section 3.2.

Run#	Date	HV-M	HV-D	Conn	Pitch	Strip	MM Evts	SI Evts	Gas	Chamber Name
4134	11/20/09	550	850	2	500	250	5001	5001	Ar : CO2 (85:15)	R4
4133	11/20/09	550	850	2	500	250	5045	5045	Ar : CO2 (85:15)	R4
4132	11/20/09	530	830	2	500	250	5055	5055	Ar : CO2 (85:15)	R4
4126	11/20/09	570	870	3	250	150	5033	5033	Ar : CO2 (85:15)	R3
4123	11/20/09	570	870	3	250	150	5057	5057	Ar : CO2 (85:15)	R3
4093	11/19/09	500	800	11.12	250	150	2389	2389	Ar : CO2 (85:15)	R3
4088	11/19/09	520	820	11.12	1000	900	10003	10003	Ar : CO2 (85:15)	P1
4086	**11/19/09**	**510**	**810**	**11.12**	**1000**	**900**	**10053**	**10053**	**Ar : CO2 (85:15)**	P1
4082	11/19/09	500	800	11.12	1000	900	5013	5013	Ar : CO2 (85:15)	P1
4081	11/19/09	500	800	11.12	1000	900	5023	5023	Ar : CO2 (85:15)	P1
4060	11/18/09	500	800	3	250	150	5032	5032	Ar : CO2 (85:15)	P3
4056	11/18/09	500	800	3	250	150	10020	10020	Ar : CO2 (85:15)	P3
4055	11/18/09	500	800	3	250	150	10057	10057	Ar : CO2 (85:15)	P3
4054	11/18/09	500	800	3	250	150	10052	10052	Ar : CO2 (85:15)	P3
4053	11/18/09	500	800	3	250	150	10010	10010	Ar : CO2 (85:15)	P3
4052	11/18/09	500	800	3	250	150	10044	10044	Ar : CO2 (85:15)	P3
4049	11/18/09	500	800	3	250	150	10007	10007	Ar : CO2 (85:15)	P3
3984	11/17/09	530	830	11.12	1000	900	5015	5015	Ar : CO2 (85:15)	P1
3981	**11/17/09**	**540**	**840**	**11.12**	**1000**	**900**	**5004**	**5004**	**Ar : CO2 (85:15)**	P1
3980	11/17/09	540	840	11.12	1000	900	5037	5036	Ar : CO2 (85:15)	P1
3349	07/21/09	380	530	2223	250	150	10038	10038	Ar:CF4:iC4H10 (95:3:2)	P1
3339	**07/21/09**	**380**	**530**	**1516**	**250**	**150**	**10038**	**10038**	**Ar:CF4:iC4H10 (95:3:2)**	P1
3336	07/21/09	380	530	1516	250	150	10017	10016	Ar:CF4:iC4H10 (95:3:2)	P1
3333	07/21/09	380	530	1516	250	150	10019	10019	Ar:CF4:iC4H10 (95:3:2)	P1

Figure 3.19 : Micromegas data from Run Book is shown and selected runs for the calculations are marked as bold. [27]

The reason with the resistive coating is to make Micromegas insensitive to discharges induced by large energy deposition due to highly ionizing particles, and limit discharge current to avoid the high voltage break-down. There are thin layers of resistive paste on readout strips with metallic pads in Micromegas with resistive coating. Moreover, there is no high voltage drop up to high local rates and it has much better performance compared to non-resistive chamber P1 (prototype one), but there are still some technical problems with reliable electrical contacts, so the groups at CERN work on Micromegas with resistive coating.

Beam tests of a 0,5 m^2 size prototype chamber have been performed in 2009, as well as several tests with different types of resistive coating of the readout electrodes, in order to reduce sparking of the chambers. A full-size prototype (1 m^2) for the ATLAS upgrade Phase1 is currently under construction, it includes on chamber integration of the front-end and readout electronics [24,25,26].

In Figure 3.20, an example of the test beam setup is shown and the scale is in millimetre. 120 GeV pion beam is used. Firstly, the prototype of the detectors are put after the beam. Si3, Si1 and Si6 are Bonn Atlas Telescopes (BAT) which are the silicon trackers to do very precise tracking and determine the pion tracks. SA, SB, SC and SD are the scintillators and they are located on one side of the chambers that used to for trigger the readout electronics and measuring the number of incoming particles. It does not matter to put the scintillators before or after the detectors, because the time of flight is only few nanoseconds, whereas whole delay before the trigger signal arrives in readout takes many hundred of nanoseconds. The veto scintillator is used to make sure the beam is focused enough, and a finger scintillator is used to check alignment of the beam . The block diagram of the test beam electronics is shown in Figure 3.21. According to the Figure 3.21, the prototype of Micromegas detector is connected to the pre-amplifier. The pre-amplifier is connected to the FEC and then the RCU. The control computer is connected to the RCU with ethernet and it is connected to DAQ computer with the fiber cables. On the other hand, the data acquisition is ALTRO system which is developed for ALICE experiment.

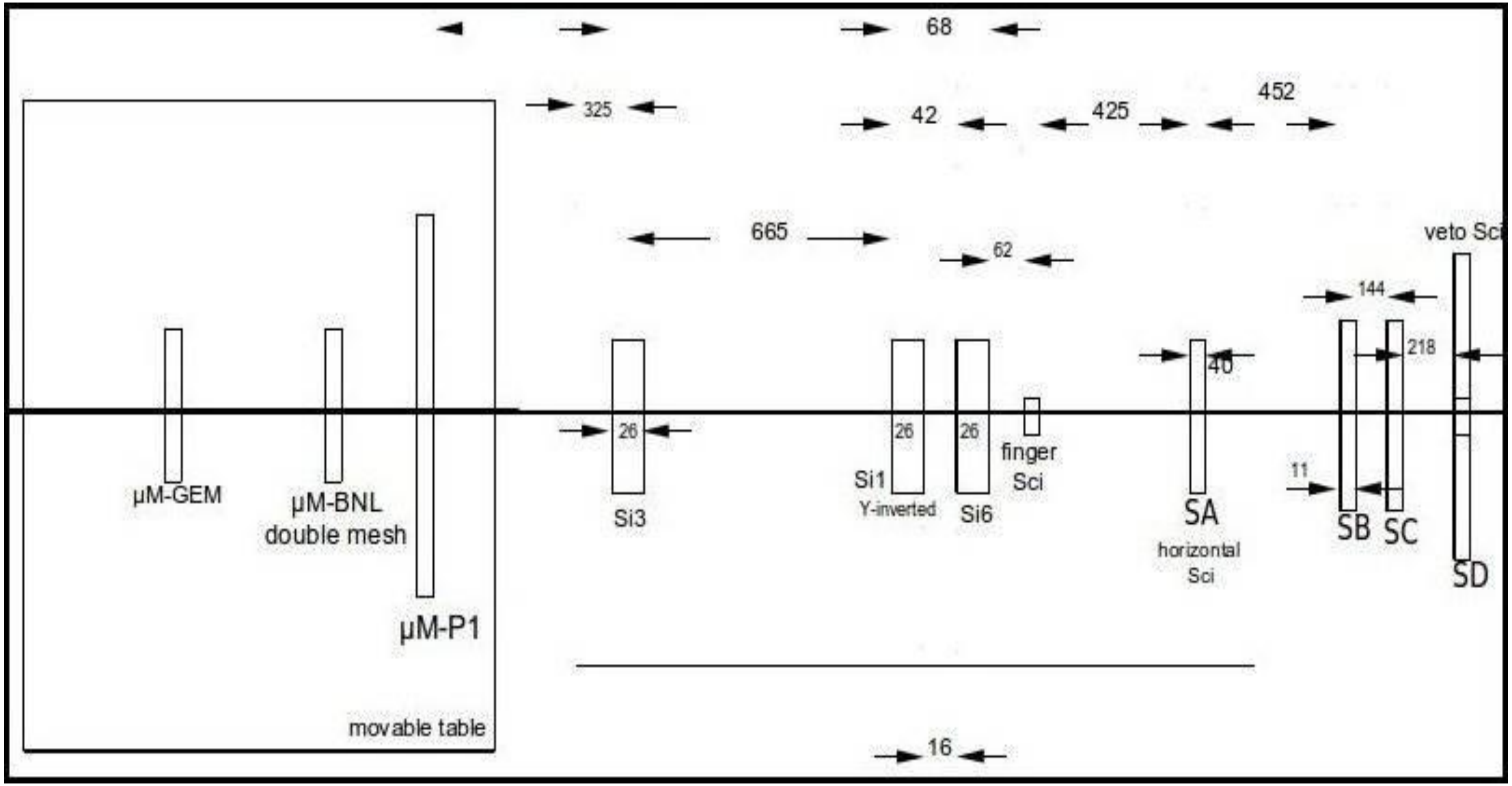

Figure 3.20 : An example of the test-beam setup.

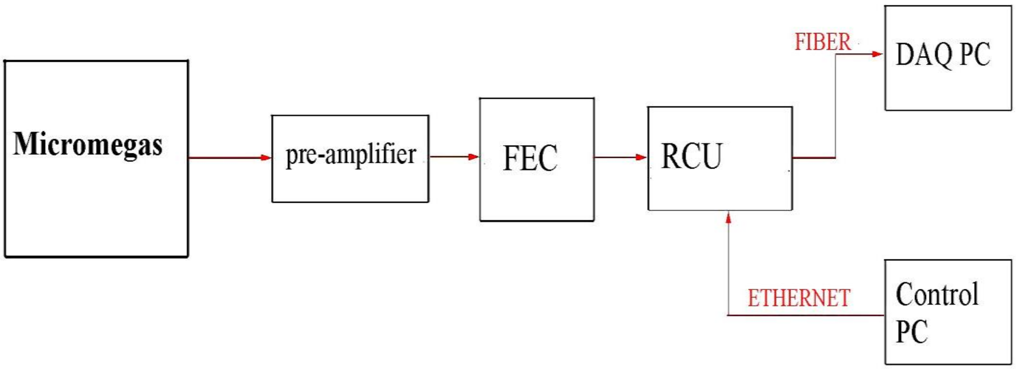

Figure 3.21 : The block diagram of the Test-beam electronics

FEC is the front-end card, and RCU is run control unit. During the test beam, 2 FECs are used and there are 32 channels in each of them. The strips which are connected to the FECs change according to the runs. For example, the 11. and the 12. strips are connected to the FECs for Run 4086 which is shown in the Table 3.18. P1 is used for this run, and the order of the strips of this prototype is shown in Figure 3.22.

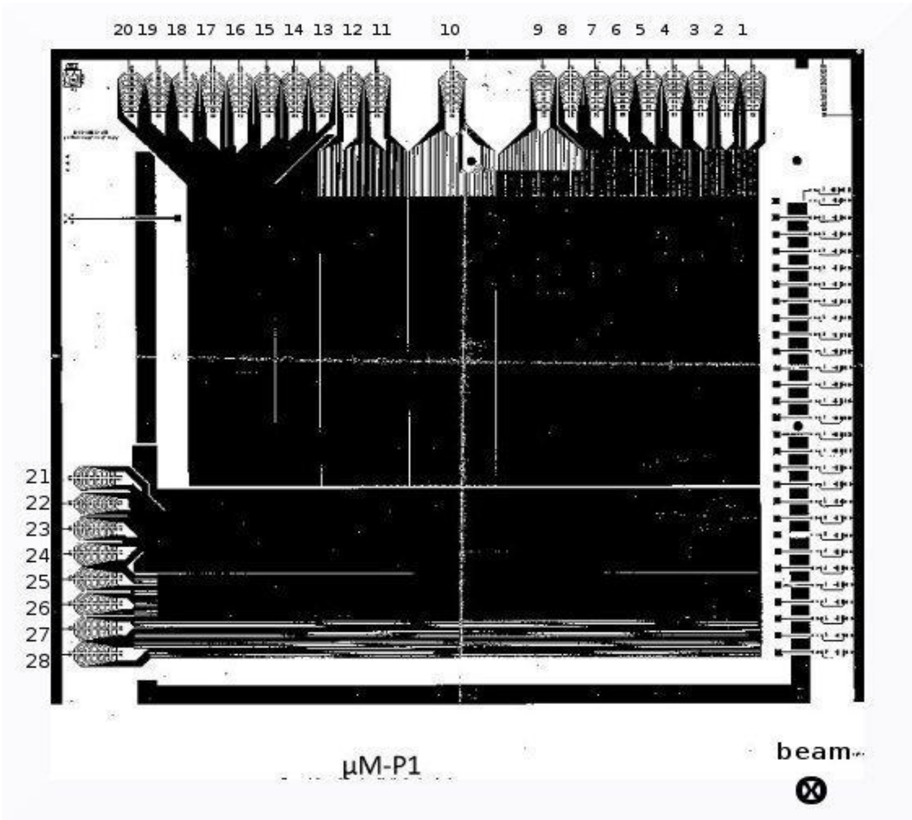

Figure 3.22 : The schematic of the strips of the P1 detector

Each strip cluster (from 1 to 28) includes 32 strips as can be seen from Figure 3.22. 32 strips are connected to the first FEC, and the other 32 strips are connected to the second FEC. The one of the strips is connected to the electronics to measure the timing information. However, there are 128 channels in total as the high gain and low gain.

There is only one physical signal that is split into two parts, a large amplitude (about 95%) that is then recorded in the high-gain channel and a small amplitude (about 5%) that is recorded in the low-gain channel.

The two channels are missing, so the data is taken from the 126 channels. One of them is the timing channel, and all the others are the channels of the strips. Therefore, one signal is taken from the timing channel for each event. Using timing channel the time difference between the trigger and the next clock cycle in the front-end card is measured. This time is then translated into a charge. The charge scale is arbitrary, the only important thing is that the smallest times correspond to smallest charge and the largest time difference possible (100 ns) corresponds to the largest charge measured. In Figure 3.23, an example of the delay between clock and trigger is shown.

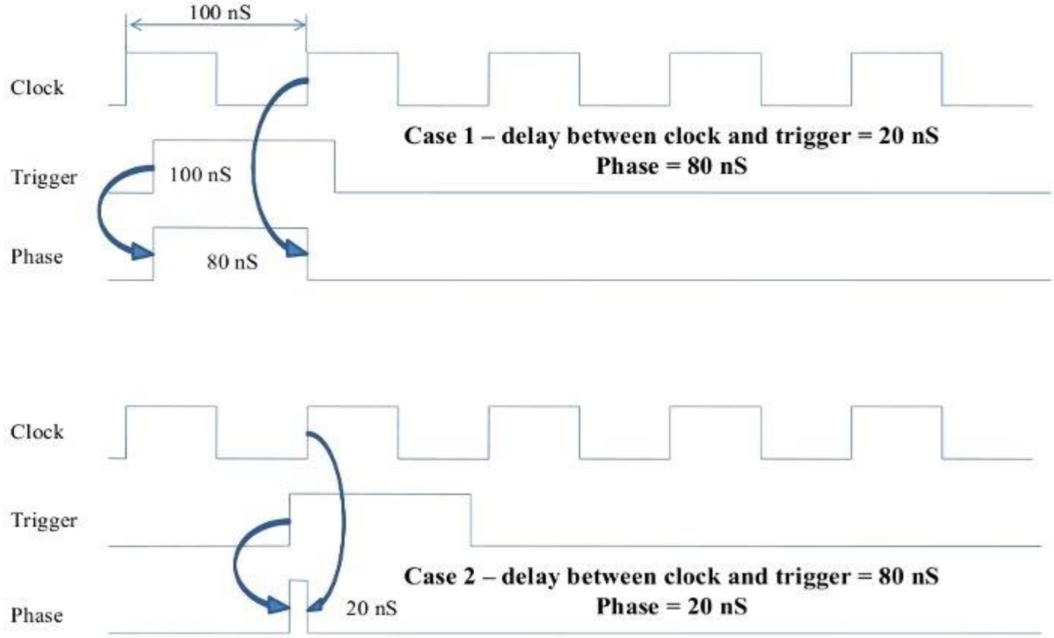

Figure 3.23 : Delay between clock and trigger

As it was mentioned earlier, there are 126 channels which the data is taken, and 65 number of samples (which is arbitrarily choosen) are collected in every 100 ns. There are 15 pre-samples (before the signal) and 40 late-samples (after the signal) to observe the possible background/pedestal, then the main signal extends over about 10 time samples.

Figure 3.24 shows an example from the Run 4086. For each event, there are 8190 samples in total which is the multiplication of the number of channels 126 and the number of samples 65 for each channel. Eventhough it looks only 3 peaks in the spectrum, since channels for low and high gains are consecutive and resolution of

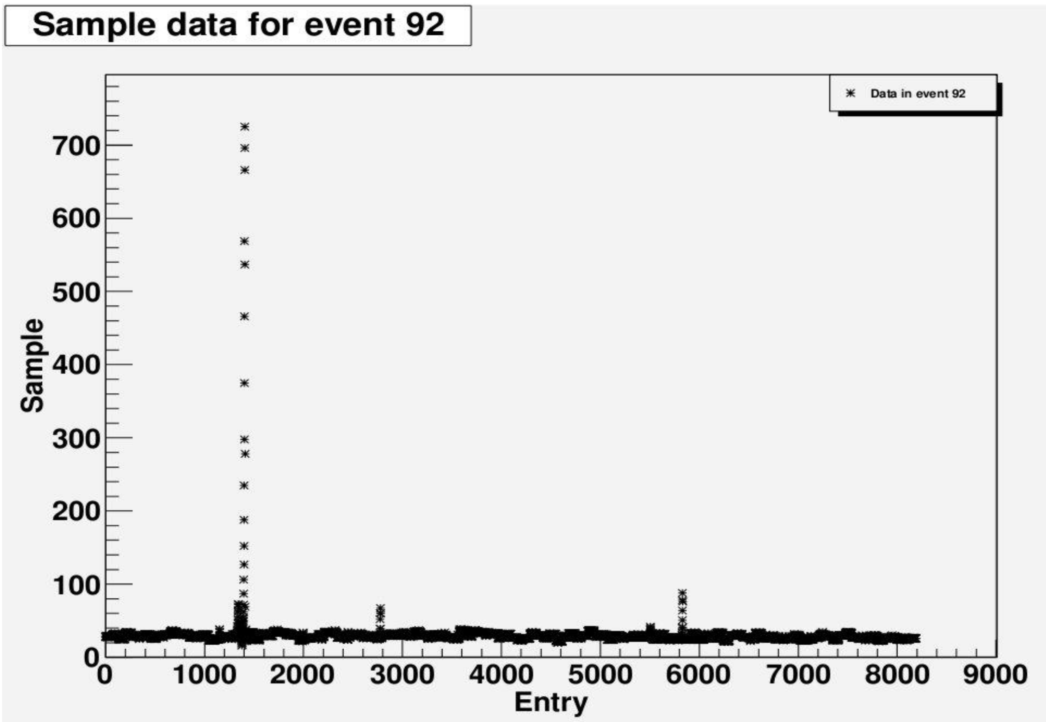

display is not enough to distinguish. For example, the timing channels are the 20^{th} and the 21^{th} channels according to the data.

Figure 3.24 : Sample data of event 92 for Run 4086

3.3.1 Gamma_2 Function

Gamma_2 function which is shown in equation 3.14 was used fitting the signal so that the each strip charge could be estimated. This function is a special function to use in the data analysis of the test-beam. In Figure 3.25, a signal for the Run 4086, Event 542, channel 20 is shown as an example. The plot shows the total charges due to the sample. There are 65 samples for each channel. The pedestal is fixed as 30.93 and the maximum charge is about 50 for this example. The trigger time is calculated by using the maximum charge value which is mentioned in 3.3.2. On the other hand, it is important to see the peak between the range that it is chosen by using the electronics.

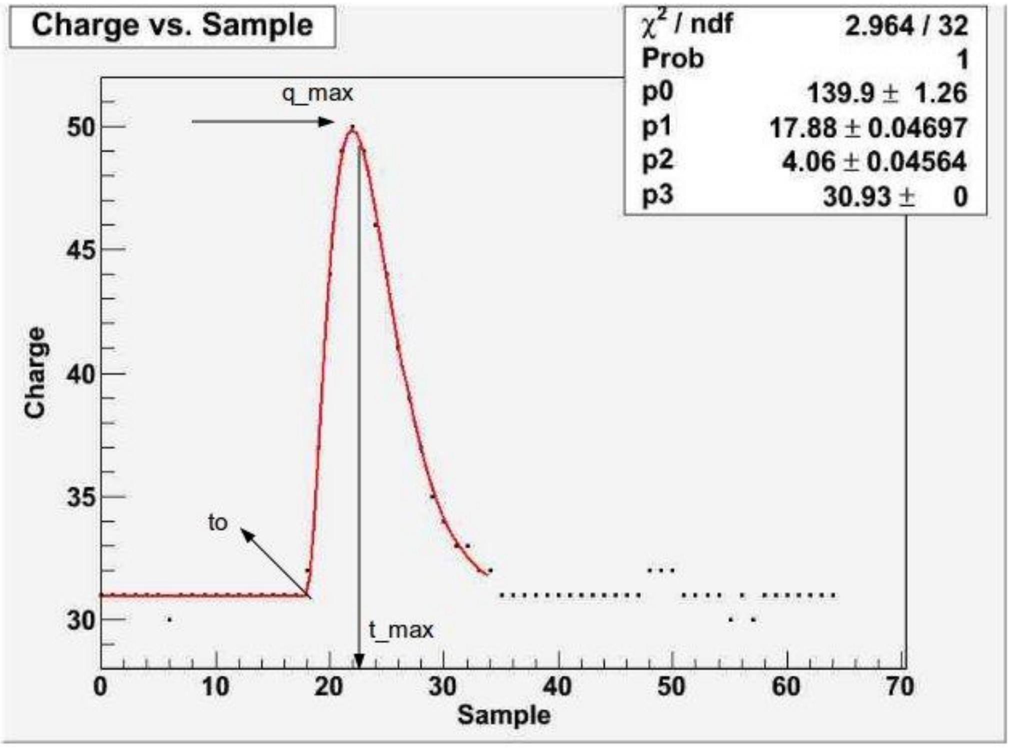

Figure 3.25 : Fitting samples for Run 4086, Event 542, channel 20

The Gamma_2 function is :

$$\begin{cases} Ped. & (t \le t_0) \\ C(\frac{t-t_0}{\tau})^2 e^{-2(\frac{t-t_0}{\tau})} + Ped. & (t \ge t_0) \end{cases} \qquad \textbf{(3.14)}$$

where t_o is the parameter p1 and it is the point where the peak starts, C is the parameter p0, τ is the parameter p2, pedestal is the parameter p3, and t is the t_max.

The first 15 samples were used to estimate pedestal and noise for each strip and each event, then the maximum sample and time were found. Strip charge is the height of the maximum point after the pedestal substraction. While using Gamma_2 function, the pedestal parameter was fixed and τ was floated. The fit was done using the first 34 samples. The half rising time $t_{0.5}$ is to reach the maximum charge with pedestal substracted.

3.3.2 The Calculation of Trigger Time

According to the Gamma_2 function, maximum value of the function can be achieved by assuming the equation **(3.15)**.

$$\frac{t-t_0}{\tau}=1 \quad \textbf{(3.15)}$$

In this case, the value of Gamma_2 function becomes as in the equation **(3.16)**.

$$(C.0{,}135)+pedestal=Q_{\max} \quad \textbf{(3.16)}$$

For the example given in Figure 3.24, for the timing channel 21, trigger time can be calculated as in the equation **(3.17)**.

$$t=\frac{q-q_{\min}}{q_{\max}-q_{\min}}.100ns \quad \textbf{(3.17)}$$

where q is the total charge in the timing channel, q_{min} is the minimum and q_{max} is the maximum charges determined from the statistical distribution after many measurement takes place for run 4086 as shown in Figure 3.26.

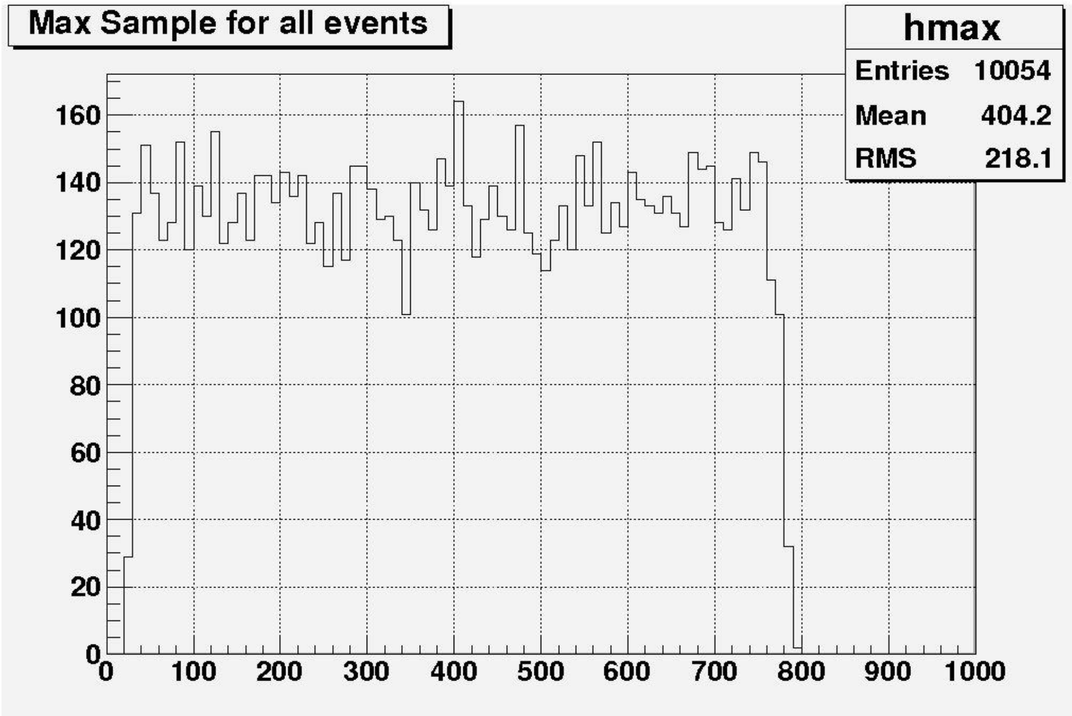

Figure 3.26 : Distribution of charges of 10054 event for Run 4086

3.3.3 The Mapping Information

The number of the strips are different from the data, and the mapping information changes for the different runs. Figure 3.27 shows the mapping information for the Run 3981 as an example. CH is the number of the channel and STR is the number of the strip. The 11th and the 12th strips were used for the Run 3981. The dead channels were 32 and 37, so there were 126 channels in total. The one of the channels refers to the timing channel.

CH.	STR.	CH.	STR.	CH.	STR.	CH.	STR.
0	15	32	31	64	47	96	63
1	15	33	31	65	47	97	63
2	11	34	27	66	43	98	59
3	11	35	27	67	43	99	59
4	18	36	2	68	50	100	34
5	18	37	2	69	50	101	34
6	22	38	6	70	54	102	38
7	22	39	6	71	54	103	38
8	21	40	5	72	53	104	37
9	21	41	5	73	53	105	37
10	17	42	1	74	49	106	33
11	17	43	1	75	49	107	33
12	12	44	28	76	44	108	60
13	12	45	28	77	44	109	60
14	16	46	32	78	48	110	64
15	16	47	32	79	48	111	64
16	3	48	19	80	35	112	51
17	3	49	19	81	35	113	51
18	7	50	23	82	39	114	55
19	7	51	23	83	39	115	55
20	30	52	14	84	62	116	46
21	30	53	14	85	62	117	46
22	26	54	10	86	58	118	42
23	26	55	10	87	58	119	42
24	25	56	9	88	57	120	41
25	25	57	9	89	57	121	41
26	29	58	13	90	61	122	45
27	29	59	13	91	61	123	45
28	8	60	24	92	40	124	56
29	8	61	24	93	40	125	56
30	4	62	20	94	36	126	52
31	4	63	20	95	36	127	52

Figure 3.27 : Mapping Information for the Run 3981

The strips which are fired in one event generate a cluster. Cluster is defined the strips adjacent to each other, and the number of the cluster should be one in the event. The size of the cluster depends on the pitch of the strips. If the pitch is smaller between the strips, the size of the cluster is bigger. On the other hand, cluster charge is a sum of the strip charges after the pedestal substraction. Cluster position is defined as peak strip position from the equation **(3.18)**.

$$x = \frac{\sum_{i=1}^{N} x_i q_i}{\sum_{i=1}^{N} q_i} \qquad \textbf{(3.18)}$$

where q is the charge and x is the number of the strip which is shown in Figure 3.26 as an example.

4. CONCLUSION

For future SLHC upgrade one of the most challenging objectives is realization of large area MPGDs. The developed Micro Pattern Gas Detectors technologies which include the GEM and the Micromegas detectors were introduced, and these detectors are the good potential candidates for the construction of large muon chambers that combine trigger and tracking capability and can sustain high particle rates expected at the SLHC.

The principle of operation of the Micromegas and GEM detectors were mentioned. The measurements and performance tests of Micromegas and GEM detectors were explained. The gain and the ratio between the electric fields of the amplification gap and the conversion gap are calculated for the Micromegas detector. The spark effect was explained, and it was determined the spark effect prevents to reach higher voltages, so the double stage amplification was offered as a solution and the measurements were done with MM + GEM detector. The voltage scans were performed step by step to understand the characteristic and performance of the detector. Moreover, the best voltages are generated to determine the optimum values for the electric fields of the drift gap and the amplification gap. The maximum gain was observed up to 10^4. The resolution of the detector was calculated as 21%. The spark probability was also measured, and the maximum voltage for the mesh was 500 V with spark effect.

The Test-beam and the detectors which are used in the Test-beam period were explained. The data analysis of the Test-beam data was explained. The fitting method was declared, and the Gamma_2 function was shown.

The different kinds of prototypes of the Micromegas detectors have been performed periodically with the beam tests. One of the possible changes in the future might be to use alternative gas mixtures in the detector, put more amplification stages, improve the resistive paste structure, etc. Moreover, a full-size prototype (1 m^2) for the ATLAS upgrade Phase1 is currently under construction, and this prototype is improved with the beam tests. On the other hand, GEM has different kinds of types and the new technologies can be improved with GEM for high energy physics, dosimetry and thermal neutron detection, medical imaging, etc.

Micropattern gas detectors are very good candidates for the construction of the large muon chambers, and for the high energy physics, medial physics, also for the future's technology and have many applications in our daily life.

REFERENCES

[1] **Magrath, C. A.,** 2009. The Heart of ATLAS Commissioning and Performance of the ATLAS Silicon Tracker, CERN-THESIS-2009-**052** , 1–2.

[2] **Url-1** <*http://lhc-machine-outreach.web.cern.ch/lhc-machine-outreach*> accessed at 29.05.2010.

[3] **Url-2 <***http://public.web.cern.ch/public/en/lhc/LHCExperiments-en.html*>, accessed at 09.05.2010.

[4] **Cwetanski, P.,** 2006. Straw Performance Studies and Quality Assurance for the ATLAS Transition Radiation Tracker, CERN-THESIS-2006-**025**, 10-15.

[5] **Bachmann, S.,** 2001. Performance of GEM detectors in high intensity particle beams, Nucl. Instr. Meth. A, **470**, 540-548.

[6] **Smith, G.C, Fischer, J., Radeka, V.,** 1988. Capacitive Charge Division in Centroid Finding Cathode Readouts in MWPCs, IEEE Trans. Nuc. Sci. NS-**35** (1), 409-413.

[7] **Mathieson, E., Smith, G.C.,** 1989. Reduction in Non-Linearity in Position-Sensitive , IEEE Trans. Nuc. Sci. NS-**36** (1), 305-310.

[8] **Rutherford, E., Geiger, H.,** 1908. An electrical method of counting the number of alpha particles from radio active substances, Proc. Royal Soc. A, **81**, 141-161.

[9] **Sauli, F., Sharma, A.,** 1999. Micro-pattern gaseous detectors. *Annual Review of Nuclear and Particle Sciende*, **49**, 341.

[10] **Charpak, G.,** 1968. Proc. Int. Symp. Nuclear Electronics, *Versailles*, 10-13.

[11] **Oed**, **A.,** 1988. Position sensitive detector with microstrip anode for electron multiplication with gases, Nucl. Instrum. Meth. A, **263**, 351-359.

[12] **Sauli, F.,** 1997. GEM: A new concept for electron amplification in gas detectors, Nucl. Instrum. Meth. A, **386** , 531-534.

[13] **Giomataris, I.,** 1996. MicroMegas: a high granularity position sensitive gaseous detector for high particle-flux environments, Nucl. Instr. and Meth. A, **376** , 29-35.

[14] **Giomataris, I.,** 1998. Development and prospects of the new gaseous detector Micromegas, Nucl. Instr. and Meth. A, **419**, 239-246.

[15] **Charpak, G., Derre, J., Giomataris, Y., Rebourgeard, P.**, 2002. Micromegas, a multipurpose gaseous detector, Nucl. Instr. and Meth. A, **478**, 18-26.

[16] **Zioutas, K.**, 2005. First results from the CERN axion solar telescope, Phys. Rev. Letters, **94**, 121-301.

[17] **Ochi, A.,** 2001. A new design of the gaseous imaging detector: Micro Pixel Chamber, Nucl. Instr. Meth. A, **471**, 248-264.

[18] **Andriamonje, S.,** 2002. Advances in Neutron Scattering Instrumentation. Edited by Anderson, Ian S.; Guérard, Bruno. Proceedings of the SPIE, **4785**, 214-225.

[19] **Giomataris, I.,** 2006. Micromegas in a bulk, Nucl. Instrum. Meth. A, **560**, 405.

[20] **Delbart, A.,** 2001. New developments of Micromegas detector, Nucl. Instrum. Meth. A, **461**, 81-84.

[21] **Url-3** <http://technologytransfer.web.cern.ch/TechnologyTransfer/en/Technology/GEM.html>, accessed at 29.04.2010.

[22] **Url-4** <http://gdd.web.cern.ch/GDD/>, accessed at 09.05.2010.

[23] **Tikhonov, V., Veenhof, R.,** 2002. Gem simulation methods development, Nucl. Instr. and Meth. A, **478**, 449-452.

[24] **Alexopoulos, T.,** 2009. The ATLAS muon Micromegas R&D project: Towards large scale chambers for the s-LHC, JINST, 4:P12015

[25] **Alexopoulos, T.,** 2009. Development of large size Micromegas detector for the upgrade of the ATLAS Muon System, Nucl. Instr. and Meth. A, **06**, 113.

[26] **Kuutmann, E. B.,** 2010. Calibration of the ATLAS calorimeters and discovery potential for massive top quark resonances at the LHC , CERN Thesis-2010-**026**.

[27] **Url-5** **<**https://apex.cern.ch/pls/htmldb_atlas/f?p=197:1:2194771168422048>, accessed at 20.12.2009

CURRICULUM VITAE

Candidate's full name : Sinem Şalva

Place and date of birth : Istanbul, 20/04/1984

Universities and Colleges attended :

2007 - 2010 Master of Science in Engineering Physics, ITU, Istanbul

2002 - 2007 Bachelor of Science in Physics, Işık University, Istanbul

1998 - 2002 High School, Kadir Has Anatolian High School, Istanbul